Oxidation behavior of candidate NiCr-alloys for engine exhaust valves - Part I: Effect of minor alloying elements

R. Pillai[a,*], M. Romedenne[a], J.A. Haynes[a], B.A. Pint[a]

[a]*Materials Science and Technology Division, Oak Ridge National Laboratory, Oak Ridge, TN 37831-6156, USA*

Abstract

Oxidation induced degradation of structural materials employed as exhaust valves within internal combustion engines (ICEs) will be a relevant life-limiting mechanism, in addition to creep and mechanical fatigue, due to ever-increasing severity of operating temperatures and pressures. Ni-Cr based alloys, which form external chromia-based scales at the relevant operating temperatures are being considered as suitable candidate materials. Thermal cycling of these alloys in water vapor containing atmospheres, such as those present during hydrocarbon fuel combustion within ICEs, can considerably influence their oxidation behavior. In this study, the role of typical alloying additions such as Mn, Si, Al and Ti on the cyclic oxidation behavior of model NiCr-X (X=Mn,Si,Al,Ti) alloys exposed in dry air and air+10% H_2O at 800 °C and 950 °C was investigated. Combined additions of Mn and Si reduced scaling rates compared to binary Ni-22Cr alloys. The presence of water vapor possibly suppressed formation of NiMnCr-spinel and thereby the Cr depletion in the alloy. Combined Al and Ti additions mainly resulted in accelerated oxidation kinetics due to the Ti-doping of chromia scales. More porous external scales were observed in water vapor leading to a much deeper depth of nitridation in the Ni-22Cr-Al-Ti alloys.

Keywords: cyclic oxidation, water vapor, Ni-based alloys, internal oxidation, alloy composition profiles, Electron back scatter diffraction

1. Introduction

Light and heavy duty automotive and truck engines are expected to operate at peak exhaust temperatures well in excess of 800 °C to meet increased efficiency requirements [1]. Oxidation induced degradation of the structural materials for certain engine components will be a relevant life-limiting mechanism at these temperatures in addition to creep and mechanical fatigue [1, 2]. Various chromia forming Ni based alloys (René41, Haynes 282, Nimonic 80A, Nimonic 90, Pyromet 31V, Inconel 751, Hastelloy X), combining excellent oxidation resistance and creep strength, are being considered as future engine exhaust valve materials. Typical engine operational cycles subject these materials to severe thermal cycling in combustion exhaust gas atmospheres, that contain up to 12% water vapor [3]. Consequently, oxidation resistance of these alloys depends on the formation, stability and adherence of chromia scales. Chromia scales are susceptible to degradation via spallation [4–6] during

*Corresponding author
Email address: pillairr@ornl.gov (R. Pillai)

thermal cycling, as well as evaporation in wet air atmospheres (O_2-H_2O mixtures) by forming $CrO_2(OH)_2$ and $Cr(O)_3$ volatile hydroxides [7, 8].

The oxidation behavior of Ni based chromia-forming alloys in dry and wet air has been widely studied [4, 6, 9–19]. Wood et al. [9] compared the oxide scale morphology and oxidation mechanisms of Fe-Cr and Ni-Cr alloys exposed to pure oxygen between 800-1200 °C. Oxidation behavior of Ni-Cr alloys was found to be more strongly dependent on the Cr content compared to Fe-Cr alloys. Douglass and Armijo [10] studied the effect of Si and Mn on the oxidation behavior of Ni-20Cr (wt.%) alloys between 1000-1200 °C. Formation of an outer MnCr-spinel ($MnCr_2O_4$) was observed on the alloys with 1 wt.% Mn. Additions of 3 wt.% Mn resulted in precipitation of an $MnCr_2O_4$ layer at the oxide-alloy interface. Discontinuous SiO_2 layers were observed at the oxide-alloy interface in alloys with 1 wt.% Si, but became a continuous layer in alloys containing 3 wt.% Si. Long-term oxidation behavior of 24 superalloys (Ni-base, Co-based and Fe-based) with varying Cr contents in static air between 850-1150 °C was reported by Angerman [11]. Gleeson et al. [4] studied the role of alloy composition on the spallation behavior of chromia scales on commercial, high-temperature chromia-forming HR-120 (0.6 wt.% Si), HR160 (2.75 wt.% Si), and H230 (0.5 wt.% Si) alloys during thermal cycling (30 day cycles) in static dry air for 720 days at 982 °C and 360 days at 1093 °C, 1149 °C and 1204 °C. Lanthanum addition (0.2 wt.%) in H230 was found to partially inhibit scale spallation and ensure formation of a semi-protective chromia scale during subsequent oxidation while the higher Si content of 2.75 wt.% in HR160 was found to result in increased scale spallation due, in part to, the much lower coefficient of thermal expansion of silica compared to the alloy, but also supported re-formation of a chromia scale. The high Fe-containing alloy ($\sim$ 33 wt.%) HR120 demonstrated the poorest oxidation resistance due to the formation of less protective Fe-rich oxide scales after spallation of the chromia scale.

The influence of the partial pressure of oxygen on chromia scale growth was investigated by Zurek et al. [13] by exposing Ni–25Cr-X (X=Mn, Y) model alloys in Ar–O_2 and Ar–H_2–H_2O at 1000 °C and 1050 °C. Chromia scaling rates were found to be accelerated in the H_2O-containing gas (low p_{O_2}) but the chromia scales adhered better in this atmosphere. The authors showed via O-isotope tracer studies that the chromia scaling mechanism shifted from outward growth in the high p_{O_2} gas to primarily inward growth in lower p_{O_2}. Y additions were shown to have a negligible influence but Mn was observed to reduce scaling rates in the low p_{O_2} gas. Hansel et al. [15] studied the effect of the ratio of H_2 to H_2O on the chromia scale growth on Ni-25Cr model alloys. The authors discussed the role of H in supporting oxide growth in the pores at the oxide/alloy interface and the interaction between H-defects and Cr interstitials affecting transport properties within chromia scales formed on Ni-25Cr. Multistage oxidation studies on a Ni-25Cr model alloy were conducted by Simon et al. [16] and demonstrated the influence of an in-situ change of gas composition on chromia scale morphology. Single stage exposure in Ar–O_2 resulted in voided and poorly adherent chromia scales while a dense well adherent chromia scale was observed to grow in Ar–H_2O. Two stage exposures by switching the gas from Ar–O_2 to Ar–H_2O and vice-versa resulted in layered scales with each layer corresponding to the scale morphology of the single stage tests.

Deodeshmukh and Srivastava [18] studied the oxidation behavior of precipitation strengthened alloys Haynes 282, René-41, Alloy 263 and Waspaloy during a year-long (360 days) exposure in flowing dry air at 871 °C. Internal attack (oxidation and nitridation) was found to be a more significant contributor to material degradation than metal loss due to external scale formation.

The effect of gas flow rates and specimen geometry on the oxidation behavior of alloy 625 in air+6%H_2O was investigated by Huczkowski et al. [19]. The authors observed a significant increase in chromium loss with increasing gas flow rates with the maximum Cr loss observed at the leading edge of the specimens.

Although, oxidation behavior of NiCr alloys has received abundant attention in the literature, investigations including the combined effects of thermal cycling and water vapor, relevant to the operational cycles of internal combustion engines are lacking. Furthermore, an improved understanding of the role of alloy composition over a wider temperature range under these conditions is essential to enable development of application specific strategies for alloy design for high temperature components. The current work is the first part of a two-part combined experimental and computational study on the high temperature oxidation behavior of candidate NiCr-base alloys for engine exhaust valves under conditions relevant to light and heavy duty internal combustion engines. In Part I of this study, the role of typical alloying additions such as Mn, Si, Al and Ti on the oxidation behavior of model Ni-22Cr-X (X=Mn, Si, Al, Ti) alloys exposed in dry air and air+10% H_2O between 800-950 °C was experimentally investigated. The model alloy compositions discussed here are qualitatively representative of commercially relevant materials for engine exhaust valves. The results will be discussed in terms of measured compositional evolution in the alloy and oxide scale microstructures. Thermodynamic interactions between the alloying elements will be used to support the discussions. Part II will discuss the results of coupled thermodynamic-kinetic modeling to interpret the experimental observations reported here. Additionally, the applicability of the modeling approach to predict oxidation induced lifetime of commercial NiCr-alloys typically employed in engine exhaust valves under engine relevant operating conditions will also be discussed in Part II.

2. Experimental procedure

2.1. Materials and high temperature exposures

All of the model alloys were inductively melted and cast at Oak Ridge National Laboratory. After casting, the material was hot rolled at 1050 °C down to a thickness of about 8 mm and subsequently annealed at 1050 °C for 1 h in high purity Ar. Measurement of grain sizes were performed in accordance with the ASTM E112 procedure. Measured dimensions (length and breadth) were converted to equivalent diameters assuming a circular grain. The average grain diameter in the alloys was about 80 μm with a standard deviation of 36 μm. The chemical compositions of the studied alloy are given in Table 1. Alloy coupons ($\sim$ 10 x 20 x 1.5 mm) were ground to a 600-grit finish and ultrasonically cleaned in acetone and methanol prior to exposure. Alloy specimens were exposed in dry and wet air in automated cyclic rigs [20] whereby the samples were hung from alumina rods with platinum wire and exposed for 1 h in the hot zone followed by 10 min cooling in laboratory air to less than 30 °C after being automatically pulled from the furnace. The gas flow rate was maintained at 500 cm^3 min^{-1} (0.60-0.68 cm s^{-1} gas velocity) for both environments during the cycle. Exposures with water vapor were conducted by flowing the gas at 500 cc/min through an alumina tube that was placed inside a resistively-heated tube furnace. Distilled water was atomized into the flowing gas stream above its condensation temperature and heated to the reaction temperature within the alumina tube. Water was collected and measured after flowing through the tube to calculate its concentration and calibrate the amount of injected water

at 10±1 vol.%. High temperature exposures were conducted at 800, 850, 900 and 950 °C but results for the lowest and highest temperatures are presented in the paper. Specimen mass changes were measured after every 20 cycles for the first 100 h and then after every 50 cycles using a Mettler-Toledo model XP205 balance, with an accuracy of ±0.04 mg or ±0.01 mg cm^{-2}.

Table 1: Composition of studied model alloys (in wt.%) analyzed by inductively coupled plasma–optical emission spectrometry (ICP–OES) and combustion analysis for carbon.

Composition	Ni	Cr	Mn	Si	Al	Ti	C
Ni-22Cr (NC)	78.0	21.9	< 0.002	0.003	0.005	0.003	< 3 ppm
Ni-22Cr-Mn-Si (NCMS)	76.9	21.2	1.4	0.5	< 0.002	< 0.002	170 ppm
Ni-22Cr-Al (NCA)	76.3	21.7	< 0.002	0.003	1.98	< 0.002	22 ppm
Ni-22Cr-AlTi (NCAT)	75.2	21.9	< 0.002	0.003	1.94	0.95	36 ppm

2.2. Microstructural analyses

After oxidation tests, specimens were Cu-plated and sectioned for metallographic analyses. The mounted samples were ground to 1200 grit with SiC grinding papers and subsequently polished with diamond pastes to 1 μm surface finish. The final polishing step was made using colloidal SiO_2 slurry.

Specimens were characterized using Scanning Electron, Back-scattered Electron (BSE) Microscopy (TESCAN MIRA3 SEM), energy dispersive X-ray spectroscopy (EDAX Octane Elect Super Silicon Drift Detector) to take images and measure element concentration profiles. Electron backscatter diffraction (EBSD) was employed to obtain more detailed information on the microstructure and compositions of oxide scales. The EBSD band contrast images and phase maps were attained using the TESCAN MIRA3 SEM equipped with an EDAX Velocity Plus EBSD camera, and the TEAM EBSD software package from EDAX. Large (85 x 70 μm, 0.2 μm step) and small maps (20 x 20 μm, 0.02-0.06 μm step) were taken using 10 ms dwell time.

Image analyses was performed on the BSE images by integrating a customized Python code with the open source image analysis software ImageJ [21].

3. Experimental results

3.1. General remarks

Since the experimental observations demonstrated a qualitatively similar trend at all temperatures with increasing temperatures mainly accelerating the underlying mechanisms, the current paper is focused on the results of exposures at the lowest (800 °C) and highest (950 °C) temperatures. Exposures in dry air and air+10% H_2O will be referred to as dry air and wet air respectively hereafter. The model alloys will be designated as NC (Ni-22Cr), NCMS (Ni-22Cr-Mn-Si), NCA (Ni-22Cr-Al) and NCAT (Ni-22Cr-Al-Ti) in the text hereafter.

3.2. Oxidation kinetics

At 800 °C, all model alloys displayed similar oxidation kinetics in dry and wet air except NCAT, which showed a relatively higher mass change in wet air (Figure 1a). NCA showed the lowest mass gain among all model alloys at 800 °C. After exposure for 500 h at 950 °C NC lost significant mass and the specimen exposed in wet air showed much higher mass loss (-72 mg cm^{-2}) than the specimen exposed in dry air (-40 mg cm^{-2}) as can be seen from Figure 1b. NCMS started losing mass slightly in wet air compared to the dry air specimen while NCA gained higher mass in wet air than in dry air. In contrast to the exposures at 800 °C, NCAT showed similar mass change behavior both in dry and wet air.

Calculating rate constants for specific mass change oxidation data acquired under conditions of evaporating and spalling external oxide scales is not physically meaningful. However, it can be qualitatively useful to compare the temperature dependence of the oxidation rates for the investigated alloys. In the present work, the mass change values after 40 h of exposure was considered to estimate parabolic oxidation constants k_p assuming that the effects of evaporation and spallation would be minimal. Figure 2a shows k_p of the model alloys for exposures in dry air between 800-950 °C. In accordance with mass change, NCA specimens showed the lowest values of k_p at all investigated temperatures. Values of k_p for exposures in wet air are shown in Figure 2b. A typical temperature dependence was not observed for NC specimens. NCMS specimens showed a similar temperature dependence in dry and wet air. Higher values for k_p were observed for NCA specimens at 900 °C and 950 °C in wet air. Except at 800 °C, similar values of k_p were found for NCAT specimens in dry and wet air.

3.3. Oxidation behavior

A compact external Cr_2O_3 scale was observed on NC specimens at 800 °C both in dry and wet air (Figures 3a and 3b). The Cr_2O_3 scale constituted of smaller grains (0.3 ± 0.2 μm) after exposure in wet air than in dry air (1.5 ± 0.5 μm) at 800 °C, as Figure 4 shows. The chromia scale grown in wet air showed a two-layered structure with a finer outer and coarser inner scale. However, a thick external layer of NiO was observed followed by a heterogeneous oxide layer interspersed with Cr_2O_3 and Ni-rich oxide underneath on NC after 500 h at 950 °C in dry and wet air (Figures 5a and 5b). In case of NCMS, qualitatively similar oxide scales were observed at 800 °C and 950 °C in dry and wet air: external MnCr-spinel on top of a Cr_2O_3 scale followed by an extremely thin silica layer underneath, that was continuous in some locations (Figures 6 and 7). The external spinel at 950 °C additionally showed the presence of Ni as can be seen from Figure 7b. Locally, formation of MnCr-spinel at the chromia-alloy interface was also observed in the alloy at 950 °C in wet air (Mn EDS map in Figure 7b)). A relatively thin external Cr_2O_3 scale compared to NC, NCMS and NCAT was observed on the NCA specimens at 800 °C in dry and wet air (Figure 8). An extremely thin alumina layer, mainly continuous, formed underneath this external scale and was followed by sparsely distributed internal alumina precipitates. The maximum depth of internal oxidation at 800 °C was measured to be 6 ± 2 μm. Internal oxidation of Al was more pronounced at 950 °C in dry and wet air but a continuous layer of alumina was not observed underneath the external Cr_2O_3 scale Figure 9. Furthermore, a NiCr-spinel was detected on top of the chromia scale (Figure 9b).

Figure 10 shows that a thin alumina layer formed underneath the external chromia scale in the NCAT specimens exposed in dry air at 800 °C with internal oxide precipitates (mainly Al_2O_3) at grain boundaries. Furthermore, a continuous layer of

alumina was not observed in the NCAT specimens exposed in wet air while Al oxidized internally although at some locations the network of alumina precipitates were spaced closely enough to form a layer like structure. Ti oxide was seen mainly on top of the chromia scale in dry air and additionally as small internal oxide precipitates tens of microns below the surface in the NCAT specimen exposed in wet air at 800 °C. At 950 °C, Al and Cr oxidized internally while Ti-oxide was found primarily on top of the chromia scale both in dry and wet air (Figure 11).

A closer observation of the subsurface region of NCAT specimens exposed at 800 °C and 950 °C led to the identification of Ti-rich nitrides under the internal oxidation zone as marked in the Figure 12a and b based on EDS elemental maps (Figure 13). The measurements of the depths of internal oxidation and nitridation for the model alloys at 800 °C and 950 °C in dry and wet air are summarized in Figure 14 and Figure 15. The difference in depths of internal oxidation and nitridation at 800 °C between dry and wet air were statistically insignificant. A slightly larger depth of internal oxidation was observed for dry air exposures while a deeper penetration of nitrides was measured in wet air in NCAT at 950 °C.

3.4. Oxidation-induced alloy compositional changes

Figures 16-19 show measured EDS line profiles in the specimens. Wet air exposures were observed to accelerate Cr depletion in the NC alloys at 800 °C as shown in Figure 16a. The NC specimen exposed in wet air for 500 h at 800 °C showed the most Cr depletion with a measured Cr concentration of about 7 wt.% at the oxide-alloy interface. Dry air exposure resulted in an interfacial Cr concentration of about 13.5 wt.% in the NC specimen. At 950 °C, the interfacial Cr concentration in NC specimens was about 6 wt.% after exposure in wet air compared to about 10 wt.% after dry air exposure.

A slightly deeper Cr depletion profile was measured for the NCMS specimens in wet air compared to dry air that corresponds well with the depth of measured Mn depletion in NCMS at 800 °C (Figure 17a). In contrast, a deeper Cr depletion profile was measured in dry air compared to in wet air at 950 °C. Depth of Mn depletion in NCMS under similar conditions is about 50 μm (Figure 19) which again corresponded well with the depth of Cr depletion (Figure 18a).

Relatively flat Cr-profiles were measured in the NCA specimens exposed in dry and wet air at 800 °C with similar interfacial Cr concentrations close to 20 wt.%. Similar depths of Al depletion of about 10 μm were observed for NCA specimens exposed in dry and wet air (Figure 17b). Flat Cr profiles, mainly in the alloy subsurface, were was also observed for the NCA specimens exposed in dry and wet air at 950 °C, as is evident from Figure 18b. In contrast to the exposures at 800 °C, a larger depletion of Cr was measured for the NCA specimens exposed in wet air than in dry air (Figure 18b) with a measured interfacial Cr concentration of about 15 wt.% compared to about 20 wt.% in dry air. This was accompanied by a slightly deeper depletion of Al in dry air (Figure 19b) that agrees well with a larger depth of internal oxidation measured for NCA measured in dry air (Figure 15).

A steeper Cr profile was measured for the NCAT specimen exposed in wet air compared to in dry air at 800 °C (Figure 16b). In case of the specimen exposed in dry air, a relatively flat Cr concentration profile, as in the case of NCA specimens, was measured closer to the oxide-alloy interface. A larger depth of Cr depletion was observed for the specimen exposed in dry air (20 μm) than in wet air (10 μm). The interfacial Cr concentration value of 12 wt. % was however lower in wet air than in dry

air (about 15 wt. %). Like in the case of NCA specimens, a slightly larger depth of depletion was measured for Al in the NCAT specimens exposed in dry air than in wet air. Similar to the exposures at 800 °C, the specimen exposed in dry air at 950 °C showed a deeper Cr depletion than in wet air. Interestingly, the interfacial Cr concentrations were similar at about 15 wt. %. A slightly deeper depth of depletion of Al was measured in dry air than in wet air at 950 °C (Figure 19b), which like in the case of NCA specimens, agreed well with the larger depth of internal oxidation measured in dry air (Figure 15). In contrast to Al, Ti was observed to be depleted to a depth of about 110 μm in the NCAT specimen exposed in wet air compared to a depletion depth of about 80 μm in the specimen exposed in wet air (Figure 19b).

4. Discussion

4.1. Binary NiCr alloy

The NC specimens showed higher mass gain than the NCMS and NCA specimens but lower than the NCAT specimens at 800 °C both in dry and wet air. Significantly higher mass gains were measured for the NC specimens at 950 °C in dry and wet air followed by considerable mass loss after exposure for about 100 h in dry air and 50 h in wet air. At both temperatures, initial stages of oxidation on NC specimens will be governed by growth of NiO before the chromia layer forms underneath. At the higher temperature of 950 °C, the combined effects of oxide spallation and evaporation led to a faster consumption of Cr to form the chromia scale than at 800 °C that resulted in a critical depletion of Cr at the oxide-alloy interface. Beyond this juncture, formation of a chromia scale cannot be sustained and the alloy will transition to forming NiO scales leading to formation of much thicker and less adherent external oxide scales. The formation of NiO however will lead to consumption of Ni and simultaneous enrichment of Cr at the oxide-alloy interface. This combined with the expected drop in p_{O_2} at the oxide-alloy interface, given by the NiO-alloy equilibrium, allows reformation of chromia at the NiO-alloy interface. Presence of a multilayered oxide scale (NiO:NiCr-spinel:Cr_2O_3) on NC at 950 °C in both atmospheres confirms this mechanism of continued spallation and re-healing.

4.2. Mn and Si additions

The NCMS specimens showed lower mass gain than the NC specimen at 800 and 950 °C both in dry and wet air in the initial stages of oxidation (first 20h) (Figures 1a and b). This effect was accelerated at 950 °C and is evident by the much higher mass gain of the NC specimen compared to that of NCMS after 20 h. Formation of a MnCr-spinel and Ni, Mn and Cr-spinel ((Ni,Mn)Cr_2O_4) on top of a chromia layer was observed on the NCMS specimens at 800 °C and 950 °C respectively both in dry and wet air (Figures 6 and 7). This is in accordance with previous observations for Mn-containing NiCr alloys [10, 22–25]. An interesting observation in the current work is that the spinel formed on NCMS at 800 °C is MnCr-rich while a Ni,Mn and Cr-rich spinel was observed at 950 °C. This difference will be discussed further in this section.

Spallation of the oxide scales was observed on the NCMS specimens after 500 h at 950 °C both in dry and wet air (not shown here). The lower mass gain values for the NCMS specimens exposed in wet air at 950 °C compared to that in dry air can be attributed to the additional oxide loss induced by volatilization of chromia scales in the presence of water vapor [7, 26].

The significantly higher mass loss of NC specimens compared to NCMS specimens at 950 °C indicates that the chromia scale growing under the NiCrMn-spinel on NCMS was more adherent than the most likely chromia scales that would have formed on NC before transitioning to NiO scales, as described in section 4.1. In the case of NCMS, the presence of the NiCrMn-spinel seemed to alleviate the effects of spallation and evaporation since a chromia scale continued to form in this case even after 500 h at 950 °C.

Formation of a chromia scale under the initially formed Ni-rich scale would deplete the alloy subsurface of Cr. Thermodynamic calculations indicate that a drop in Cr activity corresponding to a concentration decrease from the initial 22 wt.% to 18 wt.% would simultaneously reduce the Mn activity by about 20 % at 950 °C. This increase in the driving force for Mn diffusion from the alloy core to the oxide-alloy interface combined with the fact that Mn mobility is an order of magnitude faster than Cr in the NCMS alloy (based on calculations performed with the thermodynamic (TCNI8) and kinetic databases (MOBNI4) results in a rapid enrichment of Mn at the oxide-alloy interface. The transformation of an initial transient NiO to a NiCrMn-spinel can then be expected given the rapid diffusion of Mn through the chromia scale [27].

Significantly higher Cr depletion in NC specimens (Figures 16 and 18) is mainly a result of the differences in oxidation kinetics between NC and NCMS. Additions of sufficient amounts of Si are known to result in the formation of SiO_2 underneath the chromia scale [10, 12] and typically slow down the kinetics of chromia-forming alloy scale growth [28, 29]. An almost continuous underlayer of silica (SiO_2) was observed at the chromia-alloy interface in the NCMS specimens under all conditions. This silica layer is most likely contributing to the reduction in oxidation kinetics of NCMS specimens. Furthermore, Si additions to a NiCr alloy are known to increase the diffusion coefficient of Cr in NiCr alloys [12] by about 20% at 1000 °C. In the current work, a roughly 5% and 30% increase in D_{Cr} was calculated for the NCMS alloy at 800 and 950 °C respectively. This would have contributed to the increased flux of Cr to the oxide-alloy interface. It is worth mentioning here based on available kinetic data (MOBNI4), Mn and Si are expected to diffuse an order of magnitude faster than Cr in the NCMS alloy that would in turn support the observed formation of a MnCr-spinel and an underlayer of silica.

Interestingly, a comparison of the Cr concentration profiles in case of NCMS between dry and wet air (Figures 16 and 18) shows that a higher Cr depletion was observed for specimens exposed in dry air at 800 and 950 °C. This observation is in contrast to an expected higher depletion for the specimen exposed in wet air due to the combined effects of oxide spallation and evaporation. The measured specimen mass change at 950 °C does reflect this effect with the specimen exposed in wet air showing higher mass loss. A comparison of the Mn concentration profiles of NCMS specimens exposed in dry and wet air at 950 °C shows a larger Mn depletion for the dry air exposure (Figure 19a). This seems to indicate a higher amount of Mn in the alloy was consumed to form the NiMnCr-spinel during exposures in dry air which would also result in a higher Cr consumption from the alloy.

The combined effect of p_{O_2} and Mn additions on the oxidation behavior of NiCr alloys was studied by Zurek et al. [13] during exposure of Ni-23Cr-0.45Mn (wt.%) in Ar–20%O_2 (high p_{O_2}) and Ar–4%H_2–7%H_2O (low p_{O_2}) at 1000 °C and 1050 °C. The authors observed decreased scaling kinetics in the presence of water vapor (low p_{O_2}) that they attributed to the potential segregation of Mn at oxide grain boundaries which reduced inward oxygen transport. Recently, Vayyala et al. [30] confirmed

the presence of Mn with atom probe tomography (APT) at chromia scale grain boundaries grown on a model FeCrTi alloy in Ar–4%H_2–4%H_2O at 800 °C. However, in this case the authors discussed the possibility of Mn segregation at oxide grain boundaries slowing outward cationic diffusion and accelerating inward oxygen transport. The current results provide partial evidence for the second mechanism. The presence of a MnCr-spinel at a few locations underneath the external chromia scale, in addition to the location shown in Figure 7, seemed to support the notion that outward Mn transport through the chromia scale was slower than inward oxygen transport in case of the wet air exposure. Chromia then most likely continued to grow inward under this MnCr-spinel supported by oxygen transport. This proposition however needs further verification.

Considerations must be given to the presence of NiCrMn-spinel at 950 °C in contrast to a MnCr-spinel at 800 °C. This hints that the formation of a NiCr-spinel at the initial NiO-Cr_2O_3 interface at the higher temperature transformed to a NiCrMn-spinel due to Mn diffusion from the alloy through the chromia scale. Growth of a NiCr-spinel at the NiO-Cr_2O_3 interface has been reported as mainly governed by counter-diffusion of divalent Ni^{2+} and trivalent Cr^{2+} ions in case of dense compact scales of the pure oxides [31]. Formation of a NiCr spinel between NiO and Cr_2O_3 layers was observed for NC specimens after 500 h at 950 °C Figure 5. Transformation of NiO to $NiCr_2O_4$ frees up three times the initial number of sites for Mn ions [31] and Mn ions are known to fit in both octahedral and tetrahedral sites in the spinel lattice. The observed manganese enrichment can possibly explain the filling of these new sites. One can suppose in the present work that the presence of water vapor somehow blocks these free sites and thereby reduces NiCrMn-spinel formation at 950 °C compared to in dry air.

The band contrast images of the oxide scales on NCMS shown in Figure 20a and Figure 21a and the corresponding phase map in Figure 22a reveal a predominantly columnar microstructure for the scale in dry air, whereas there was a bi-layered scale morphology in wet air with coarser columnar grains closer to the gas-oxide boundary and finer equiaxed grains near the oxide-alloy interface. A convoluted scale in dry air and a relatively flatter scale after exposure in wet air is also evident from Figure 20a. This effect has been previously observed for scales grown in water vapor and has been mainly attributed to scale growth driven by inward oxygen transport [13]. The experimental observations at 950 °C in the present work provide partial evidence for inward transport of oxygen bearing species in wet air that probably suppresses outward Mn transport and thereby reduces formation of mixed NiMnCr oxides. Detailed microstructural analyses to confirm the combined effects of H_2O and Mn additions on this change in oxidation behavior are out of the scope of this work.

4.3. Al addition

NCA specimens showed the lowest mass change at 800 °C (Figure 1). This could be attributed to the formation of an external alumina scale at some locations (not shown here) during exposure in dry air and the alumina underlayer at the chromia-alloy interface which would have slowed down scaling kinetics considerably. A semi-continuous alumina layer was observed for some NiCrAl model alloys investigated by Giggins et al. [32] betwen 1000-1200 °C. Chyrkin et al. [33] reported that the marginal alumina former alloy 602CA (Ni25Cr2.5Al) formed an external alumina layer at the lower temperatures of 800-900 °C but formed an external chromia scale at higher temperatures with Al oxidizing internally. The larger Cr depletion measured in the case of the wet air exposure of NCA at both temperatures (Figure 16b and Figure 18b) indicates the additional chromia loss

may have been due to chromia evaporation. The Cr-loss in the NCA specimens was estimated from measured Cr-profiles for all conditions and is tabulated in Table 2. Cr loss induced by evaporation of the chromia scale was theoretically calculated based on thermodynamic data by Opila et al. [8], assuming that $Cr_2O_2(OH)_2$ is the predominant gaseous species [8]. The procedure for calculating the Cr loss due to evaporation has been described in detail by Young and Pint [26]. At 800 °C, the additional Cr loss in case of the wet air exposure corresponds well with the theoretical Cr loss induced by chromia evaporation. Hence, oxide spallation behavior can be expected to be similar and most likely minimal under both conditions.

At 950 °C the Cr loss in case of the wet air exposure is significantly higher than that for the dry air exposure. The theoretical Cr loss due to chromia evaporation cannot account for this difference (Table 2). Furthermore, the NCA specimen exposed in wet air showed a much higher mass gain than the dry air specimen. One would expect that increased Cr loss due to volatilization in wet air would reduce the measured mass change. This can only indicate that the growth mechanisms of the oxide scales are substantially different, as was observed in case of the NC specimens. It is well known that the presence of H_2O increases chromia scaling rates by promoting inward oxygen transport and changing the growth mechanism from outward cation to inward anion transport [13, 34, 35]. The much thicker and compact scale on the wet air specimen compared to in dry air supports this hypothesis (Figure 9a and Figure 9b, Figure 14).

A comparison of the band contrast images for NCA show a finer grained chromia scale in wet air (0.7 ± 0.5 μm) than in dry (1.7 ± 0.5 μm) air (Figure 20b, Figure 22b and Figure 23) that further agrees well with previous observations of chromia scales in the presence of water vapor [13, 35]. The corresponding phase map shown in Figure 22b shows a more pronounced formation of voids at the oxide-alloy interface in dry air compared to in wet air. Void formation in the vicinity of the oxide-alloy interface of the chromia scales formed in dry air can lead to their spallation during cooling. Chromia scales grown in wet air are known to be more adherent than corresponding scales grown in dry air [16]. The oxide thickness calculated from the estimated Cr loss (EDS measurements) assuming a pure chromia scale was about 6.7 μm. This value is close to the measured value (7.8 ± 2 μm) which further suggests that the scale grown in wet air is less prone to spallation. Various mechanisms have been reported for the better adherence of chromia scales grown in the presence of H_2O. The most widely reported mechanism is the suppression of void nucleation and scale detachment due to oxide formation at the scale-alloy interface supported by inward oxygen transport in wet air [13, 35]. Simon et al. [16] attributed this to potentially different type of point defects governing transport mechanisms in the chromia scales in the water vapor containing environment. The differences in mechanisms of chromia scale growth between dry and wet air cannot be unequivocally identified in the present work. However, the experimental results obtained here are consistent with previously conducted studies on the role of water vapor on chromia scale growth and adhesion on NiCr alloys [13, 36].

The measured Cr concentration profiles in NCA differed from commonly observed diffusion profiles [37]. In Figures 16 and 18 Cr concentrations profiles are flatter in the alloy subsurface compared to the Cr profiles in NC and NCMS specimens at both temperature with the difference being more evident at 950 °C. A similar effect was observed by Chyrkin et al. [38] for Cr profiles during exposure of alloy 602CA (Ni-25Cr-2.5Al wt.%) in air at 1100 °C. It was shown by the authors that, in addition to the oxidation induced depletion of Cr, the internal oxidation of Al under the external chromia scale further reduces the chemical

activity of Cr and increases the driving force for Cr diffusion to the oxide-alloy interface. A similar effect can explain the observed Cr profiles in the current work. Thermodynamic calculations show that additions of 2 wt.% Al almost doubles D_{Cr} in NCA at 950 °C. Furthermore, the Cr activity was calculated to drop by about 10 % corresponding to its oxidation induced depletion in the subsurface by about 1 wt.%. Al depletion due to internal oxidation in the alloy subsurface zone, as seen in Figure 17b and Figure 19b results in a combined reduction in Cr activity by about 35 %.

Table 2: Calculated Cr loss (EDS measurements) from NCA specimens and calculated Cr loss induced chromia evaporation.

Temperature	**Dry air** (mg cm^{-2})	**Wet air** (mg cm^{-2})	**Cr loss due to evaporation** (mg cm^{-2})
800 °C	0.11	0.18	0.06
950 °C	0.57	1.68	0.13

4.4. Al and Ti additions

Combined additions of Al and Ti in NCAT were observed to alter the oxidation behavior compared to additions of only Al (NCA). Significantly higher mass gain was measured for the NCAT specimen exposed in wet air at 800 °C (Figure 1). Furthermore, the alumina underlayer observed in NCA after 500 h both in dry and wet air was more continuous and pronounced in case of the NCAT specimen exposed in dry air. The outer oxide scale was a mixed scale with TiO_2 growing on top of a Cr_2O_3 layer (Figure 10a). Formation of Ti-oxides on a chromia scale in Ni-base alloys has been previously reported [39–41] and is made possible by diffusion of Ti through the chromia scale and its high solubility in the chromia scale (about 18 at.% [42]). Ti doping of chromia scales through substitution of Cr^{3+} ions with higher valence Ti^{4+} ions generates Cr vacancies [43]. The resulting vacancies are then expected to accelerate outward diffusion of Cr along grain boundaries in the oxide and increase oxidation rates [30, 44]. In addition to causing an increased Cr loss due to evaporation, the presence of water vapor also most likely resulted in an increased inward transport of the oxidant (O, OH^{-1}) that additionally increased the oxidation rate, as has been discussed before for the other model alloys [13, 35, 36].

Surprisingly, the observed alumina underlayer in the NCAT specimens exposed at 800 °C did not reduce the mass gains as was seen for the NCA specimens. It can be hypothesized that the alumina underlayer mainly retards the growth of the chromia scale but is unable to apparently completely hinder the transport of Ti through the oxide scale that results in its incorporation in the scale and subsequent oxidation leading to the higher mass gain. The fact that the alumina underlayer in the NCAT specimen exposed in wet air is less continuous will be expected to result in increased Ti transport and larger mass gains. This has been observed in the micrographs shown in Figure 10b with evidently a higher fraction of Ti-rich oxides on the NCAT specimen exposed in wet air at 800 °C supported by the higher mass gains for this specimen (Figure 1a).

Interestingly, the measured Cr depletion profiles are characteristically different in dry and wet air in case of the NCAT specimens. The Cr concentration profile in wet air was much steeper than in dry air and the flattening of the Cr profile closer to the oxide-alloy interface, previously discussed for the case of NCA, was not observed in case of NCAT exposed in wet air. Based on the correlation provided earlier between the increased Cr flux and subsurface depletion of Al, a larger depletion of Al can be presumed for the exposures in dry air. A comparison of the Al profiles in NCAT specimens between dry and wet air at 800 °C

shown in Figure 17b confirms this. The combined effect of Ti addition and exposure to water vapor can explain the increased oxidation kinetics of NCAT at 800 °C.

At 950 °C, the NCAT specimens showed similar oxidation kinetics in dry and wet air. Furthermore, the Cr concentration profiles were, in contrast to the exposures at 800 °C, very similar for both dry and wet air exposures with flatter profiles in the alloy subsurface. However, a deeper Cr depletion was measured in case of the dry air exposure (about 70 μm compared to 45 μm). Based on the current experimental data, no definitive conclusions can be drawn about the influence of atmosphere on the temporal evolution of the compositional changes in NCAT. However, the most likely mechanisms of oxidation can be discussed based on the experimental observations.

In dry air, an increase in chromia scaling rates due to Ti additions will be expected to deplete Cr concentrations at the oxide-alloy interface faster than in NCA specimens. This will increase the tendency for internal oxidation of Al that has been observed with a much larger Al depletion in NCAT compared to NCA exposed in dry air (Figure 19b). As discussed before, this Al depletion will increase the Cr flux by raising the Cr chemical potential gradient and result in the flat Cr concentration profiles in the alloy subsurface (Figure 18b). Furthermore, thermodynamic calculations indicate that a decrease in Al activity (oxidation-induced depletion) is estimated to reduce the Ti activity in the subsurface by about 25 % and thereby the gradient in chemical potential of Ti. A combination of this increased chemical potential gradient and a slightly faster mobility of Ti than Cr in the austenitic matrix (about 30 %) would result in an increased driving force for the diffusion of Ti from the interior to the oxide-alloy interface. This would continue to support its transport thought the chromia scale and promote its oxidation at the gas-oxide interface that in turn would accelerate Cr depletion.

Inward transport of oxygen bearing species through the external scale can be safely presumed in the presence of water vapor. The band contrast images shown in Figure 21c clearly show a finer microstructure of the external scale in wet air at 950 °C (0.7 ± 0.4 μm in Figure 23) as has been observed for chromia scales exposed in water vapor containing atmospheres [13, 45]. The presence of chromium oxide at grain boundaries in the alloy subsurface at a few locations provide additional evidence for an increased inward flux of oxidants. In Ni-Cr alloys, this has been typically observed to increase chromia scaling rates [13, 35]. Furthermore, as discussed earlier, the presence of Ti in the alloy combined with evaporation of chromia scales in wet air is expected to further increase these rates. However, in the present work, a reduced Cr depletion in NCAT after exposure in wet air was observed after 500 h at 950 °C. The larger depletion of Ti and higher depth of internal nitridation in wet air provides a hint toward the reason for this. It can be hypothesized that in the initial stages of oxidation, the Cr concentration at the oxide-alloy interface drops lower in wet air than in dry air resulting in an increased transport of Ti to the oxide-alloy interface. An enhanced Ti-doping of the chromia scale will then make the scale more porous and prone to nitridation by enabling transport of N through the oxide scale [46, 47]. The low magnification band contrast images comparing the external scales on NCAT at 950 °C does reveal a more porous scale for the exposure in wet air (Figure 20c). The much faster diffusion of N than Ti will allow precipitation of Ti nitrides (Figures 12 and 13), as previously observed for NiCrAlTi alloys by Krupp et al. [48]. This will tie up the Ti in the alloy reducing its propensity to diffuse towards the oxide-alloy interface. This effect was reported by Nowak et al.[47] during exposure of René-80 in dry air and air+7% H_2O at 1050 °C. The higher depth of nitridation in dry air

than in wet air resulted in a less Ti-rich external scale. In the present work, this effect is reversed since a deeper nitridation was observed in wet air. Although a direct comparison between the present work and [47] is not possible since alloy René-80 has a much lower Cr (14 wt. %) and higher Al (3 wt. %) and Ti (5 wt. %) contents than NCAT, the reduced Cr depletion in wet air can be explained due to suppression of Ti transport to the oxide-alloy interface.

Krupp et al. [48] showed with the help of thermodynamic calculations that N solubility in the alloy increased with increasing Cr contents. The deeper internal nitridation observed in wet air (Figure 12b) results in a reduced Ti transport to the oxide and hence the lower Cr depletion in wet air (shallow depletion profile) than in dry air at 950 °C. The higher Cr content in the alloy then in turn enables a higher solubility of N supporting continued nitridation of the alloy. Based on these discussions, the potential O-uptake at 950 °C assuming formation of stoichiometric Cr_2O_3, TiO_2 and Al_2O_3 was calculated from the measured concentration profiles of Cr, Ti and Al respectively. Additionally, the uptake of N by formation of TiN was estimated from the measured area fraction and penetration depth of the nitrides (image analyses). These calculated values are tabulated in Table 3 and a good agreement between the calculated and measured total mass change was achieved.

Table 3: Calculated O and N-uptake in NCAT specimens after exposure in dry and wet air for 500 h at 950 °C.

Atmosphere	**Cr_2O_3** (mg cm^{-2})	**TiO_2** (mg cm^{-2})	**Al_2O_3** (mg cm^{-2})	**TiN** (mg cm^{-2})	**Calculated total uptake** (mg cm^{-2})	**Experimental mass change** (mg cm^{-2})
dry air	1.2	0.75	0.3	0.5	2.75	2.97
wet air	0.9	0.6	0.4	0.75	2.65	3.01

Among all the potential mechanisms discussed here, the role of interactions between oxygen, hydroxyl ions and nitrogen on their solubilities cannot be excluded. The reduced internal oxidation but deeper nitridation observed in wet air might be a result of these interactions. Furthermore, the proposed sequence of events is based on available experimental evidence after a single exposure time of 500 h and a temporal evolution of the different oxidation stages is needed to provide conclusive evidence for the mechanisms suggested here. Ultimately, the chemistry (solubility and activity) at the oxide-alloy interface will mainly be governed by the cross-interaction between the oxidants (O, OH^{-1}, N) and the alloying elements Ni, Cr, Al and Ti. These interactions are mainly unknown for a multicomponent alloy but the hypotheses proposed in the present work based on measured compositional changes in the alloy and characterization of the oxide scales do provide a partial explanation for the experimental observations.

5. Summary and conclusions

The cyclic oxidation behavior of four Ni-22Cr (wt. %) model alloys with additions of Mn+Si, Al and Al+Ti in air and air+10 % H_2O at 800 °C and 950 °C were reported. The experimental observations were discussed in terms of the measured compositional changes in the alloy and a characterization of the oxide scale morphology. In general, exposures in wet air resulted in fine grained external scales indicating inward transport of oxygen bearing species contributing to the scaling kinetics of the alloys. The main findings can be summarized as follows:

1. Ni-22Cr alloys showed rapid mass loss at 950 °C both in dry and wet air through a quick transition (< 40 h) from external chromia scale formation to fast growing Ni-rich oxides. A larger depletion of Cr was observed in wet air. A finer chromia scale was observed to grow on these alloys in wet air compared to in dry air at 800 °C.

2. Ni-22Cr-1.5Mn-0.5Si alloys formed an outer MnCr-spinel layer on top of a chromia layer in dry and wet air at 800 °C. At 950 °C, the outermost layer was observed to be a NiMnCr-spinel with chromia growing underneath. Presence of water vapor possibly reduced the free sites for Mn ions in the NiCr-spinel lattice and suppressed formation of NiMnCr-spinel and thereby the Cr depletion in the alloy. Si additions resulted in the formation a silica underlayer at the chromia-alloy interface which might have contributed to the slower oxidation kinetics compared to Ni-Cr specimens.

3. Ni-22Cr-2Al alloys formed an external chromia scale with a closed and almost continuous alumina layer underneath in dry and wet air at 800 °C. At a few locations, even an external alumina layer was observed to form. Exposure in wet air at 950 °C resulted in faster oxidation kinetics than in dry air which could be mainly attributed to inward oxide growth that consequently improved oxide adhesion and reduced oxide spallation. Flattening of Cr concentration profiles near the oxide-alloy interface was due to the increased flux of Cr supported by the internal oxidation of Al which increased the chemical potential gradient of Cr.

4. The oxidation behavior of Ni-22Cr-2Al-1Ti alloys was observed to more strongly depend on temperature and composition than the other model alloys. The highest measured mass gains among all alloys was predominantly due to the well known effect of Ti-doping of chromia scales that results in an increase in their scaling rates. Higher mass gain in wet air at 800 °C was the result of a combination of Ti addition and inward growth of the oxide scale. At 950 °C, water vapor most likely resulted in a larger Cr depletion at the oxide-alloy interface in the early stages of oxidation. This combined with internal oxidation of Al to enhance the supply of Ti to the oxide-alloy interface and promoted its transport through the oxide scale. This resulted in a more porous external scale and allowed increased ingress of N that tied up the Ti in the alloy matrix to form TiN. Consequently, the outward flux of Ti decreased over the duration of the exposure and resulted in a lower Cr depletion in wet air.

Identifying the exact prevalent oxidation mechanisms resulting from the combined effects of Mn/Si/Al/Ti additions in Ni-Cr alloys, thermal cycling and presence of water vapor require a more detailed evaluation of a wider group of model alloys under diverse test conditions (different exposure times and cycle durations). This is a subject of ongoing and future work.

Acknowledgments G. Garner and G. Cox assisted with the experimental work at ORNL. V. Cox is thanked for metallographic preparation. T. Lowe is thanked for helping with microstructural characterization. P. Tortorelli and M. Brady are thanked for their valuable comments on the paper. This research was sponsored by the U.S. Department of Energy Office of Vehicle Technologies, Powertrain Materials Core Program.

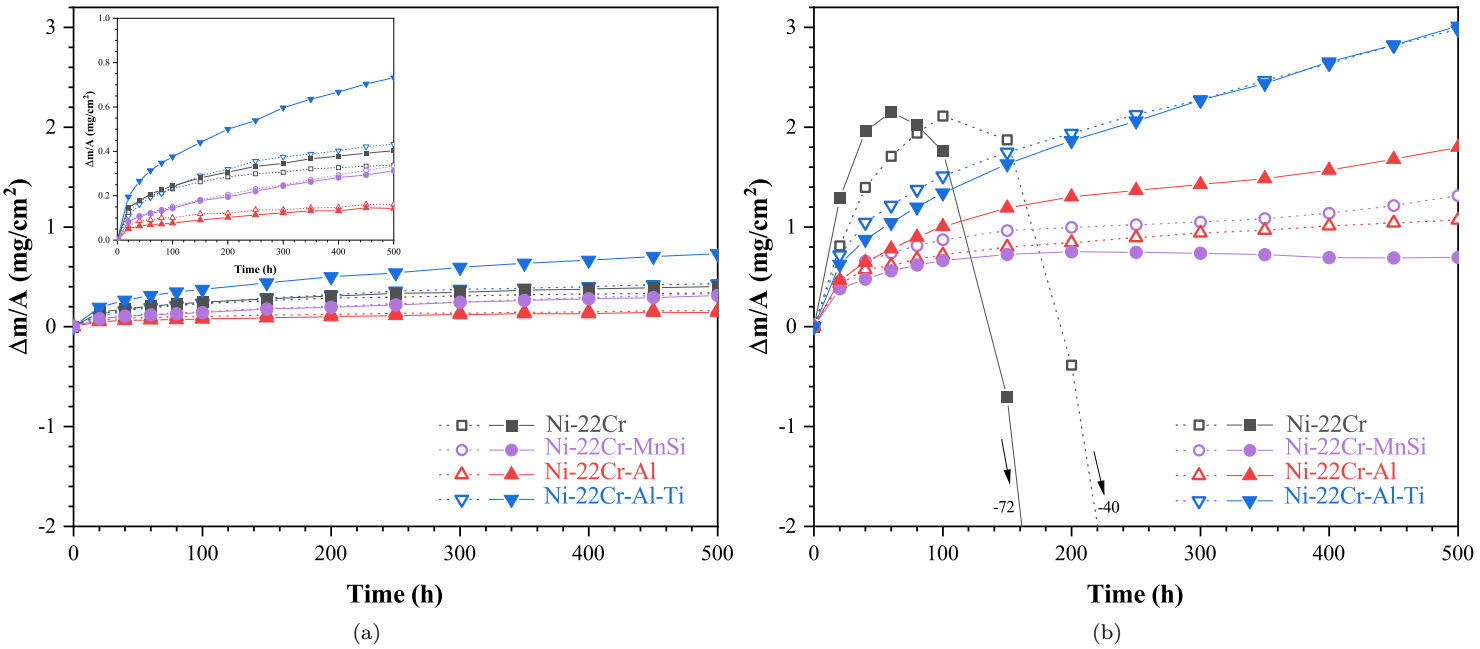

Figure 1: Mass change of model alloys as function of time in 1h-cycle dry air (open symbols) and air + 10 % H_2O (filled symbols) at (a) 800 °C and (b) 950 °C

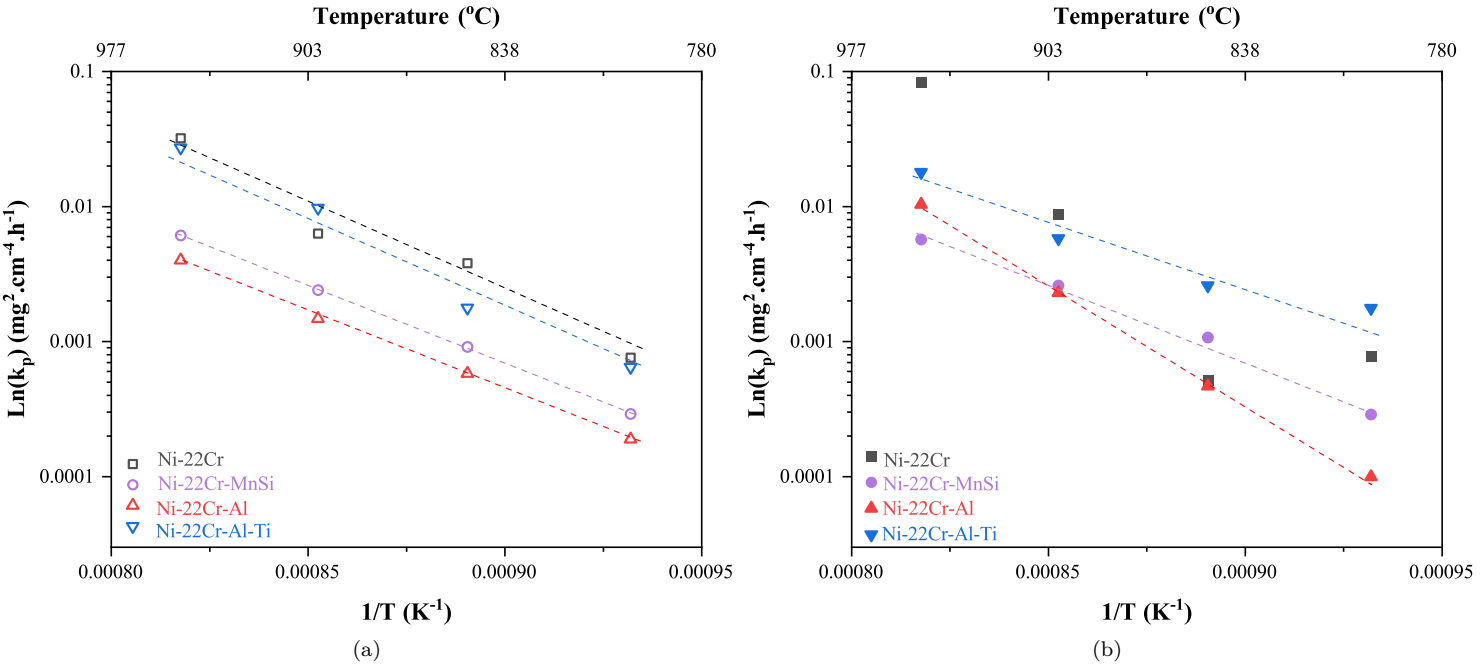

Figure 2: Oxidation rate constants (calculated after 40 h) as function of temperature after exposure in (a) dry air and (b) air + 10 % H_2O

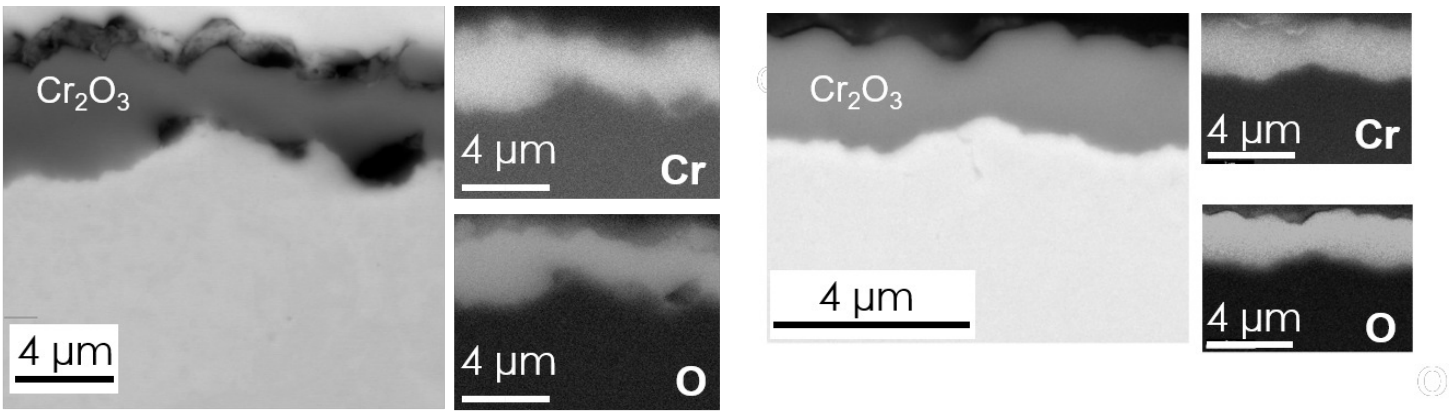

(a) (b)

Figure 3: BSE and EDS maps of Ni-22Cr after 500 h exposure in 1h-cycle (a) dry air and (b) air + 10 % H_2O at 800 °C.

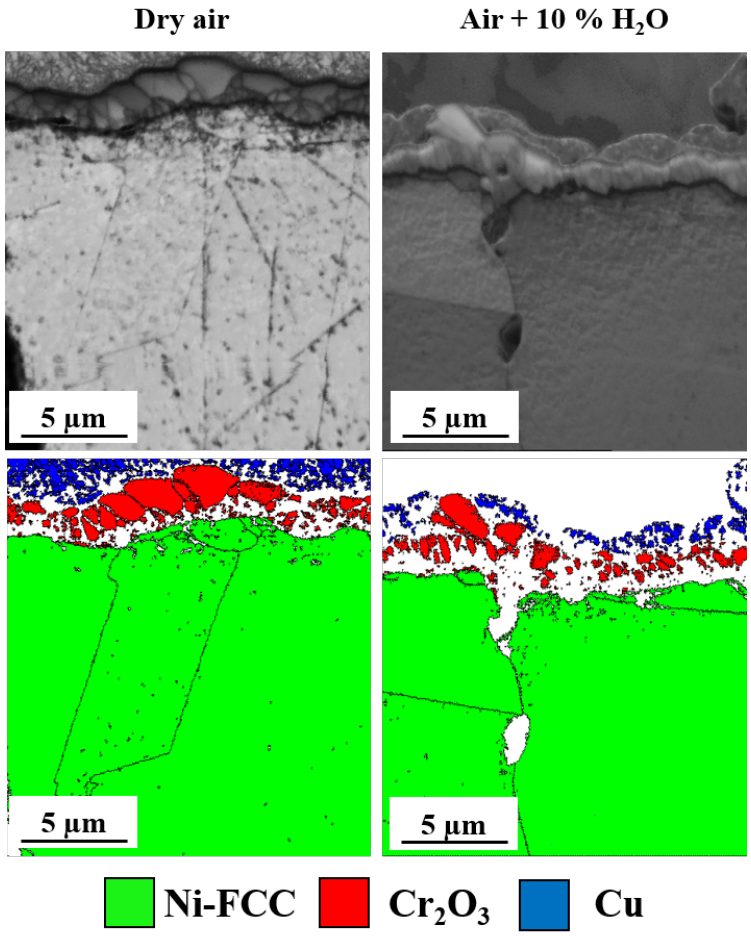

Figure 4: EBSD band contrast images and phase maps of Ni-22Cr after 500 h exposure in 1h-cycle dry air and air + 10 % H_2O at 800 °C.

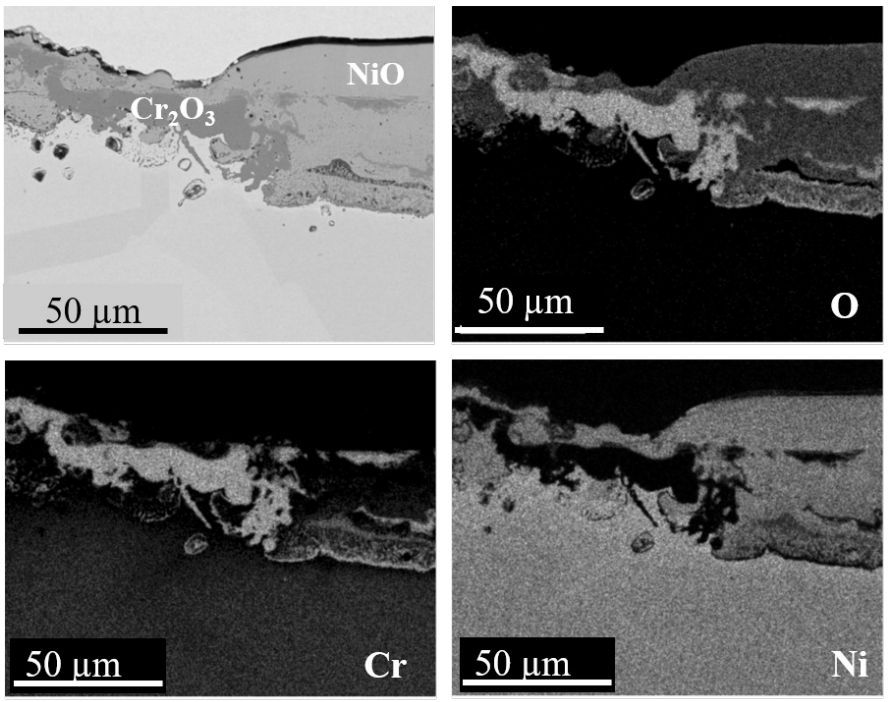

(a)

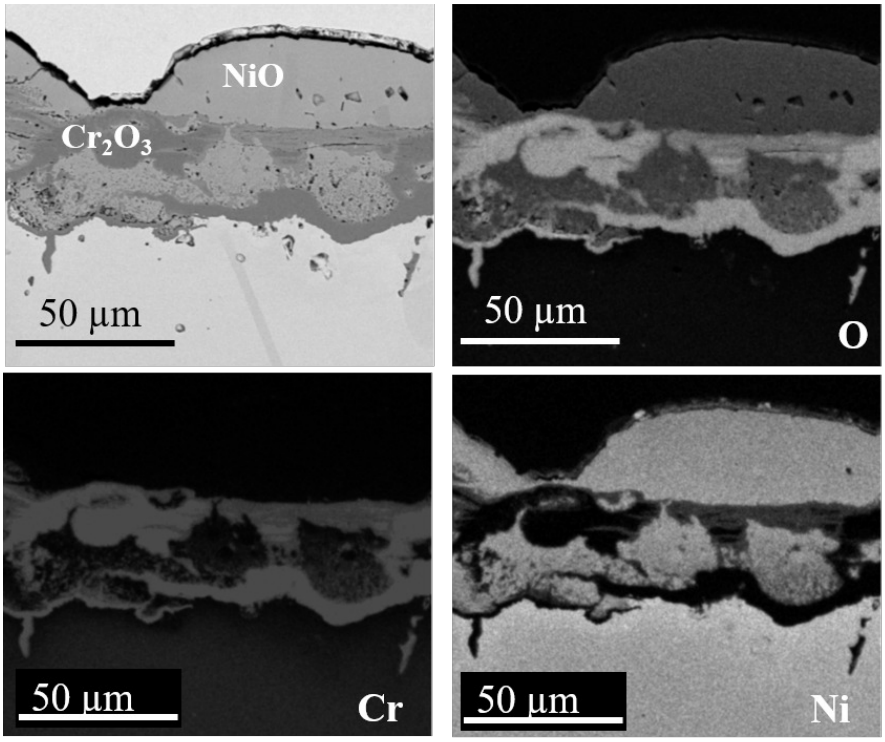

(b)

Figure 5: BSE and EDS maps of Ni-22Cr after 500 h exposure in 1h-cycle (a) dry air and (b) air + 10 % H_2O at 950 °C.

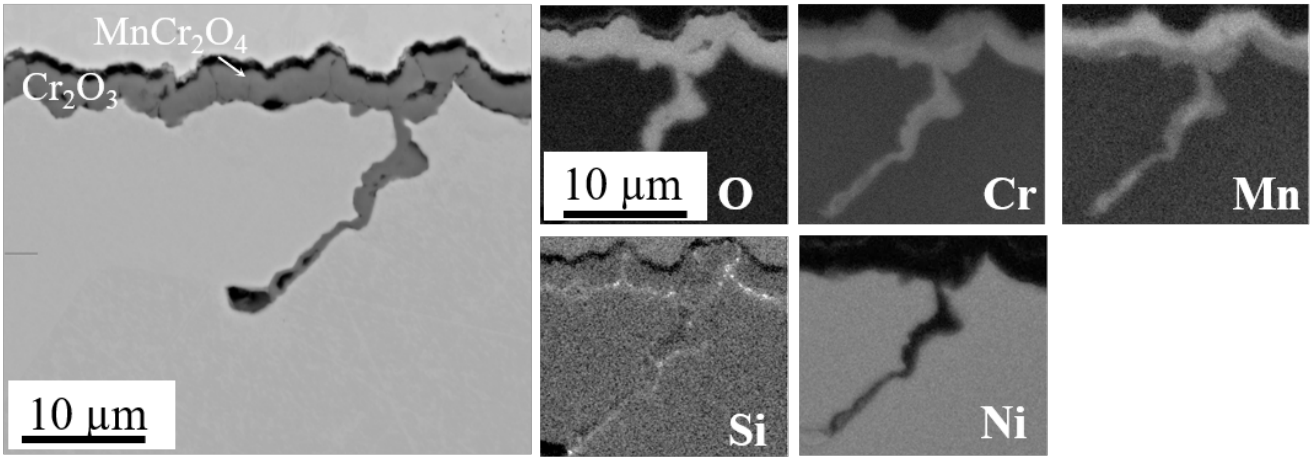

(a)

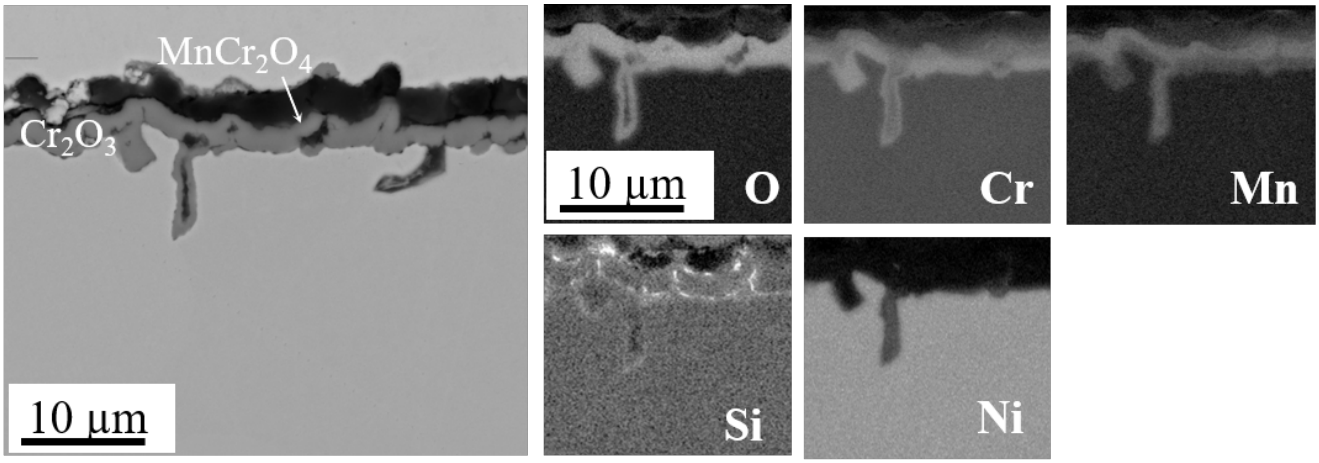

(b)

Figure 6: BSE and EDS maps of Ni-22Cr-MnSi after 500 h exposure in 1h-cycle (a) dry air and (b) air + 10 % H_2O at 800 °C.

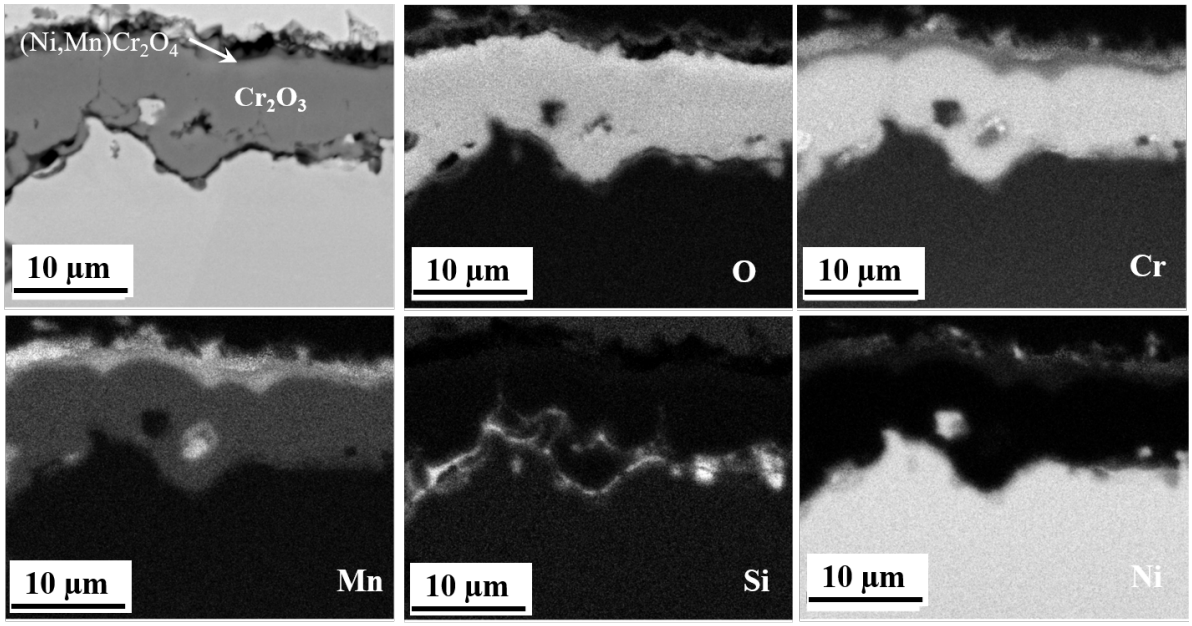

(a)

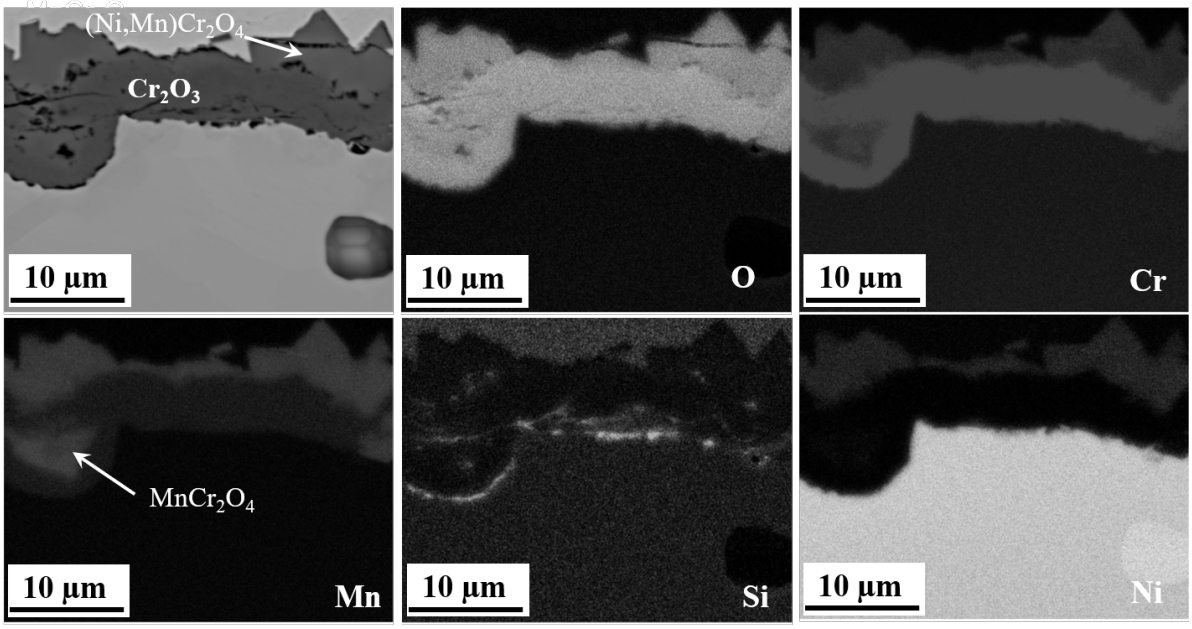

(b)

Figure 7: BSE and EDS maps of Ni-22Cr-MnSi after 500 h exposure, 1h-cycle in (a) dry air and (b) air + 10 % H_2O at 950 °C.

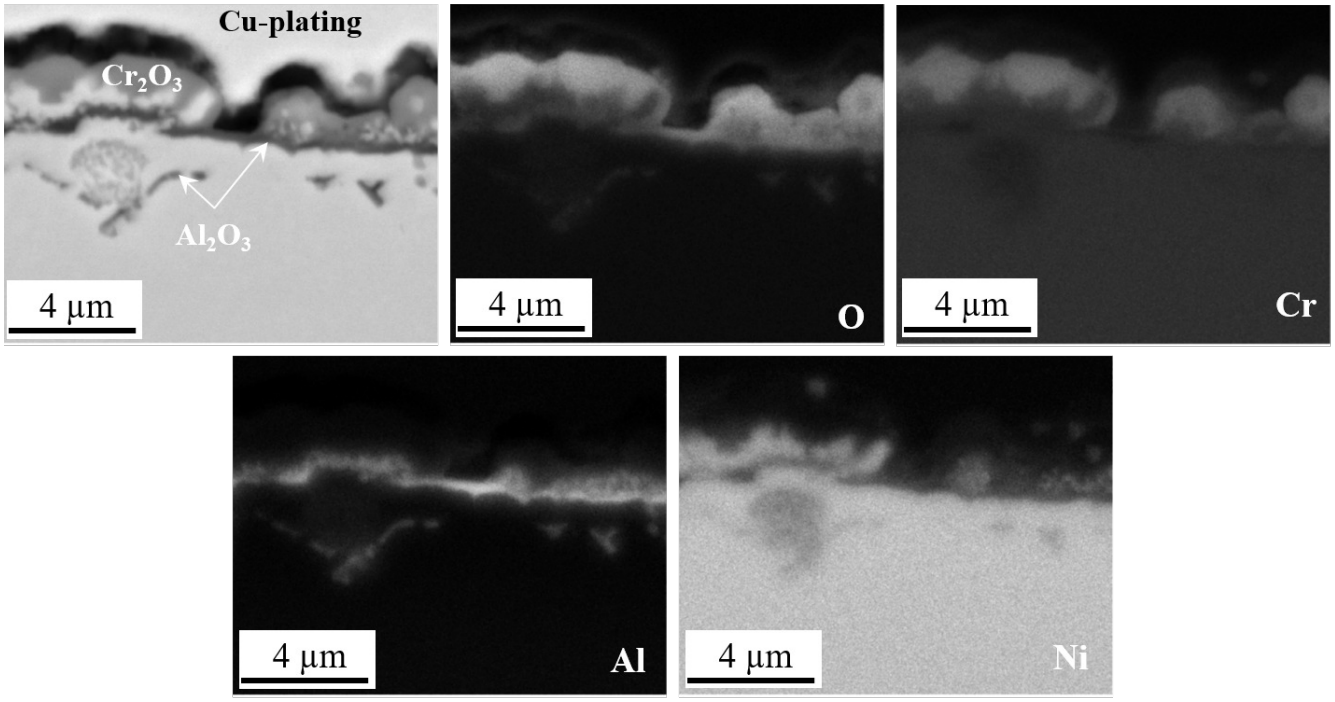

(a)

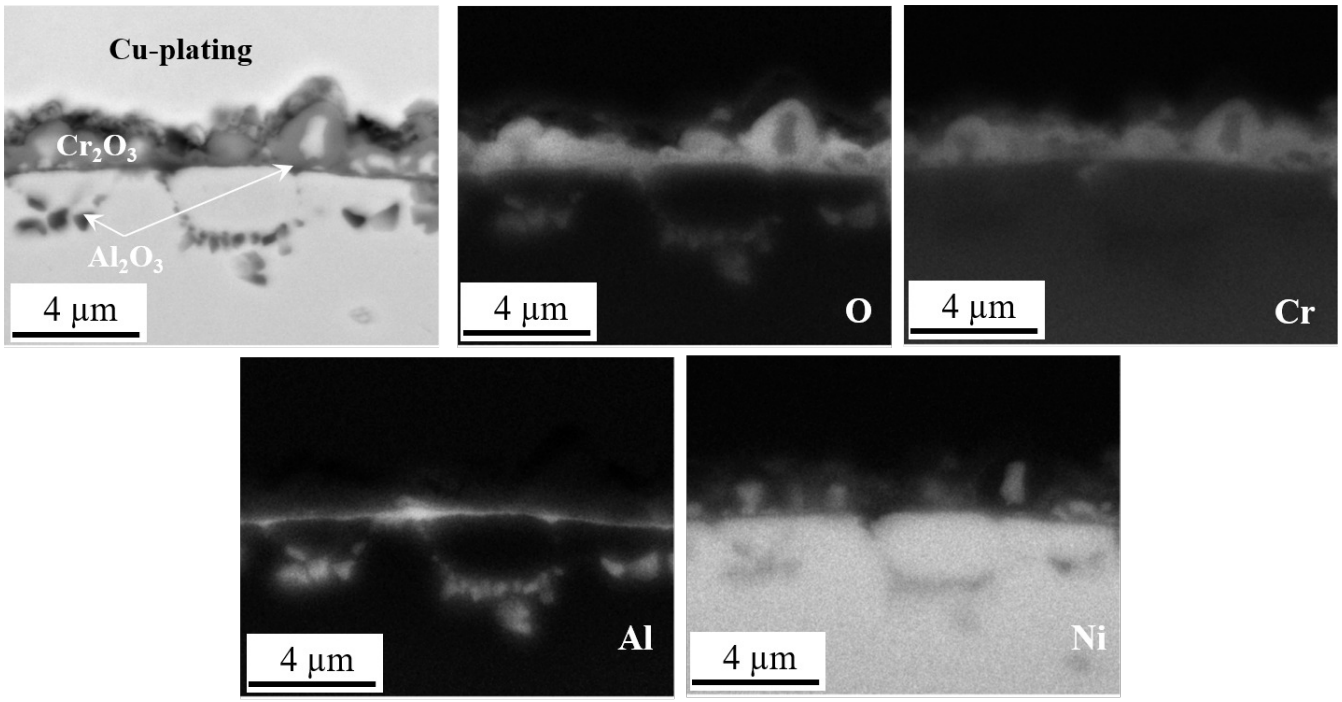

(b)

Figure 8: BSE and EDS maps of Ni-22Cr-2Al after 500 h exposure in 1h-cycle (a) dry air and (b) air + 10 % H_2O at 800 °C.

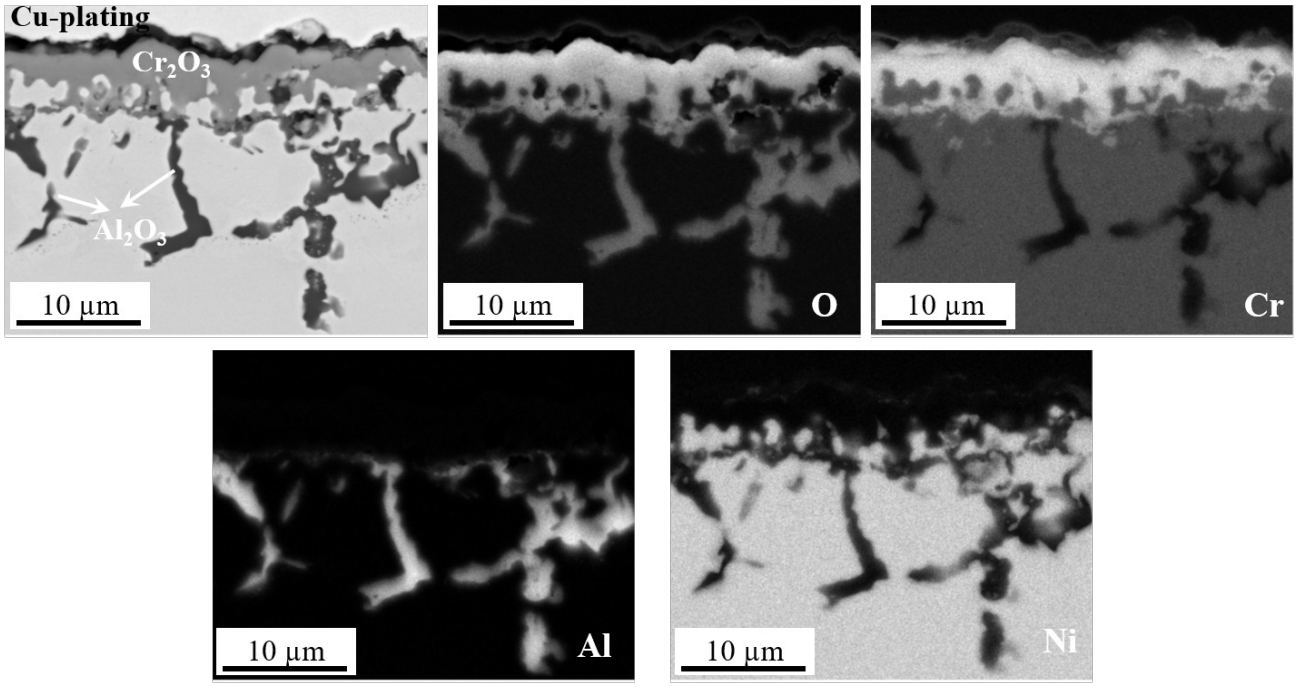

(a)

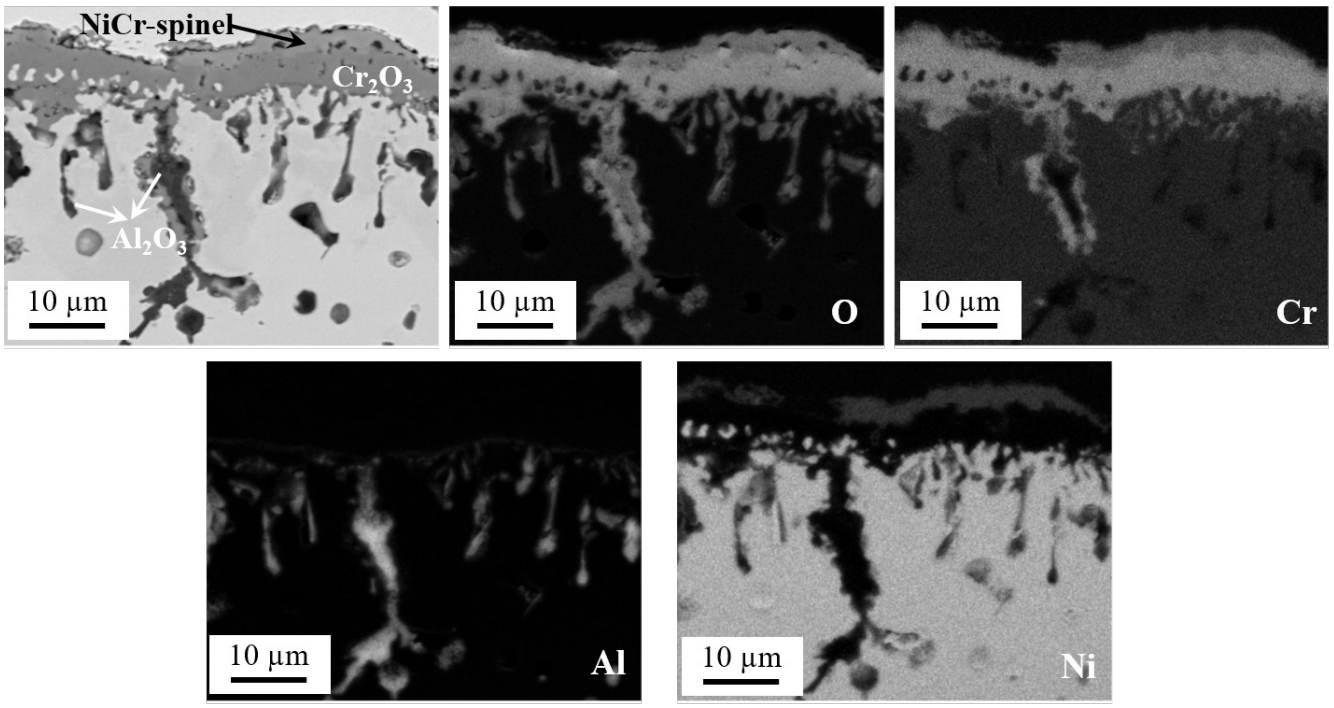

(b)

Figure 9: BSE and EDS maps of Ni-22Cr-2Al after 500 h exposure in 1h-cycle (a) dry air and (b) air + 10 % H_2O at 950 °C.

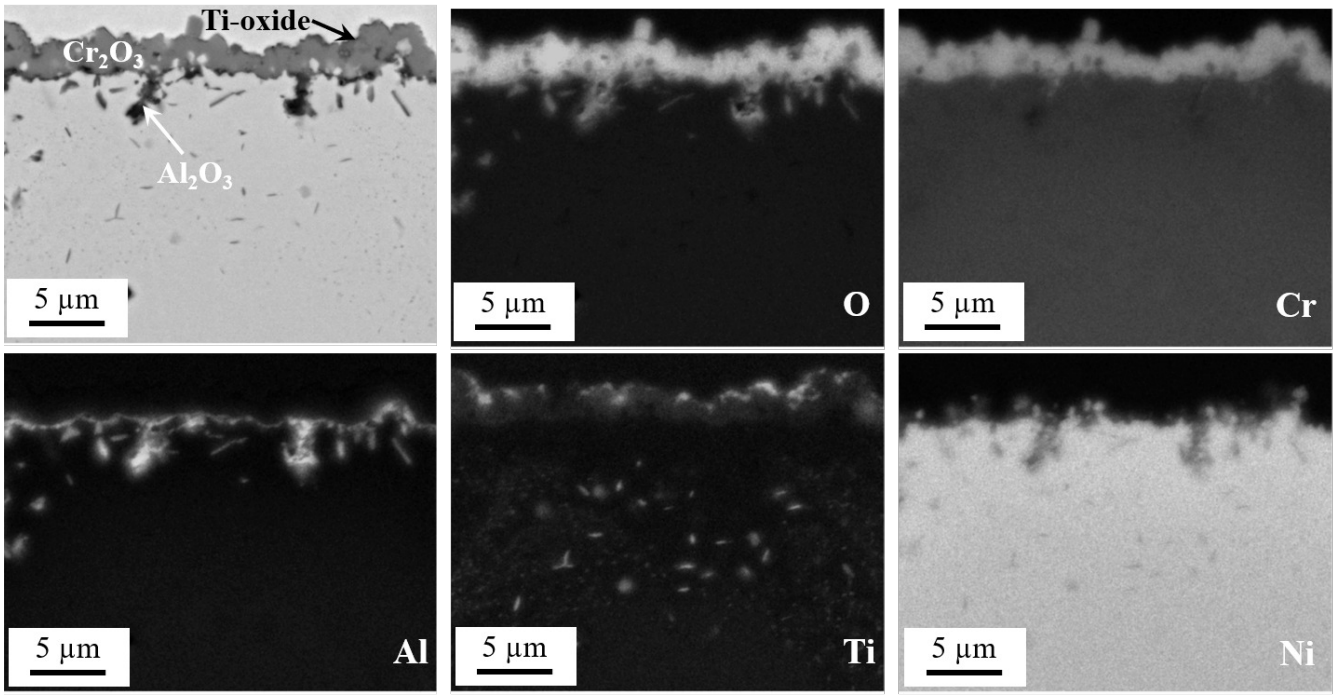

(a)

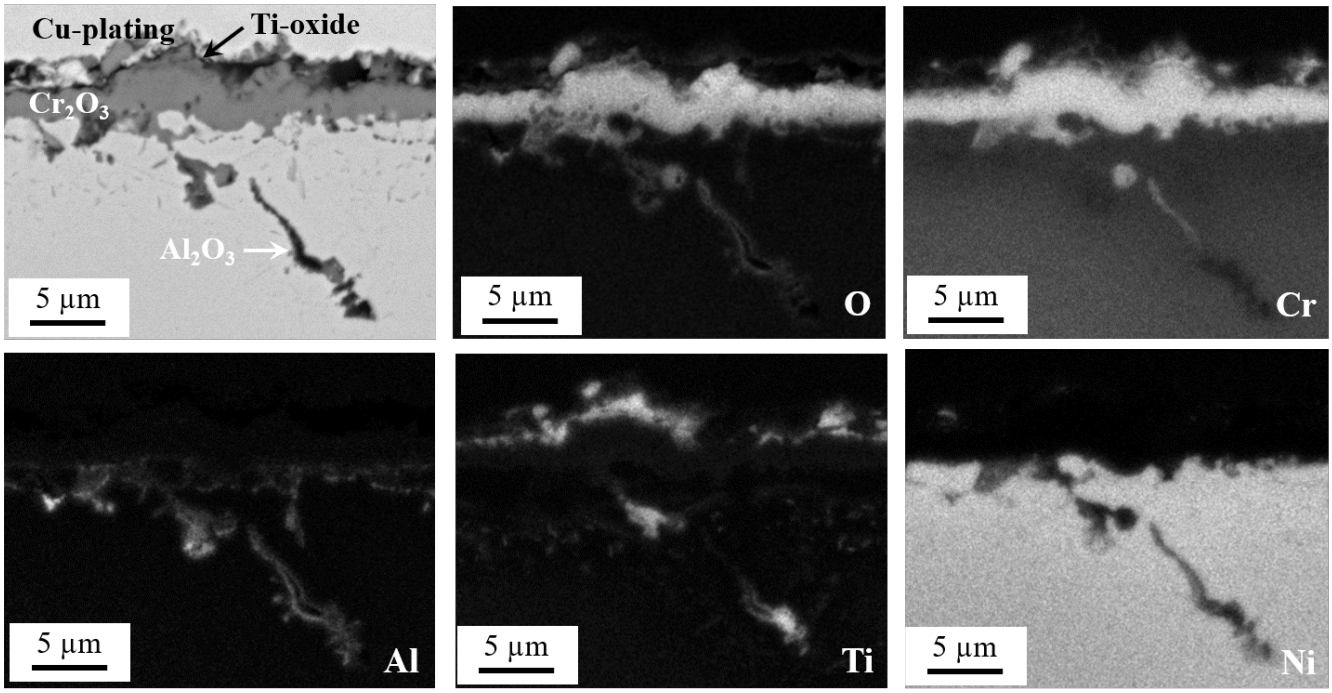

(b)

Figure 10: BSE and EDS maps of Ni-22Cr-Al-Ti after 500 h exposure in 1h-cycle (a) dry air and (b) air + 10 % H_2O at 800 °C.

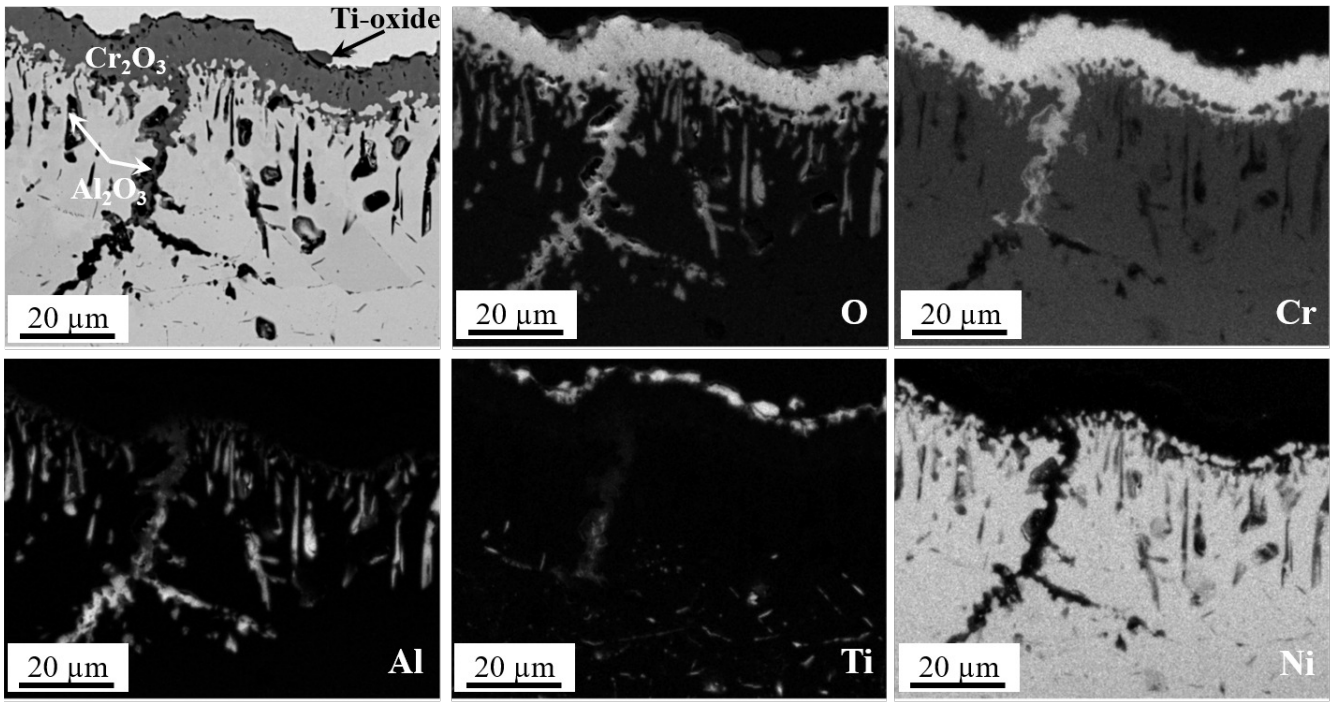

(a)

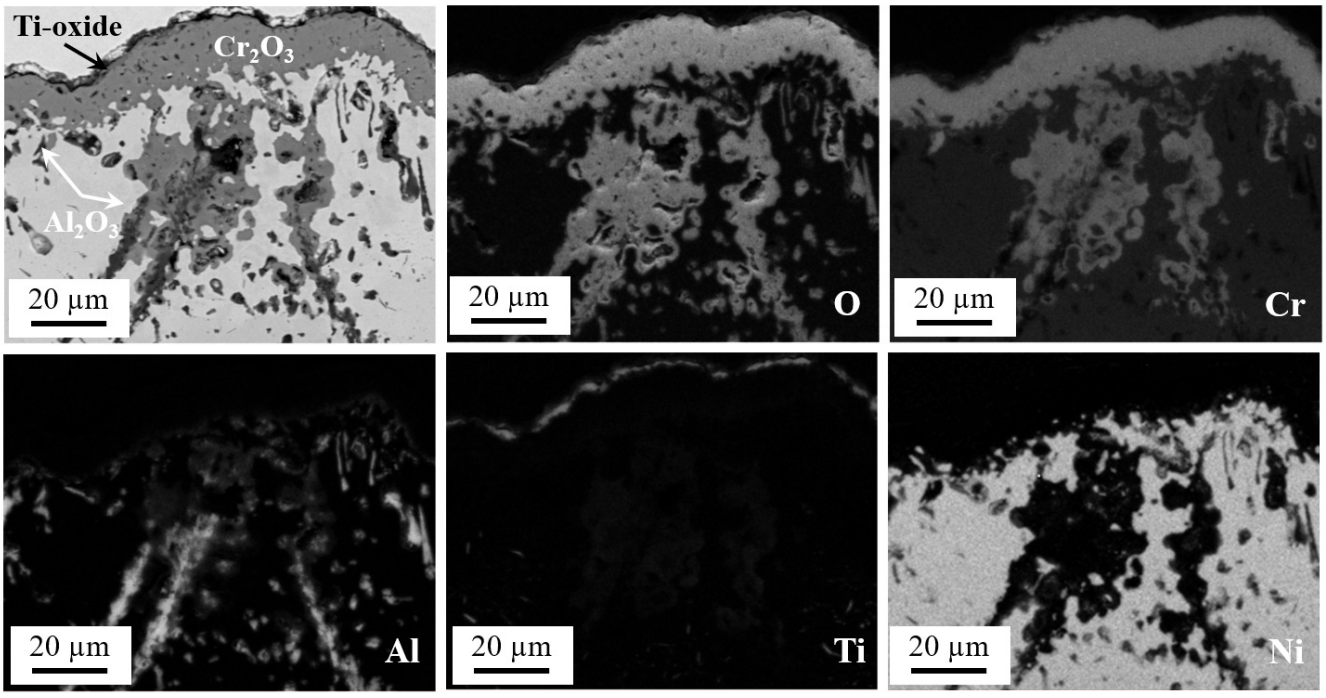

(b)

Figure 11: BSE and EDS maps of Ni-22Cr-Al-Ti after 500 h exposure in 1h-cycle (a) dry air and (b) air + 10 % H_2O at 950 °C.

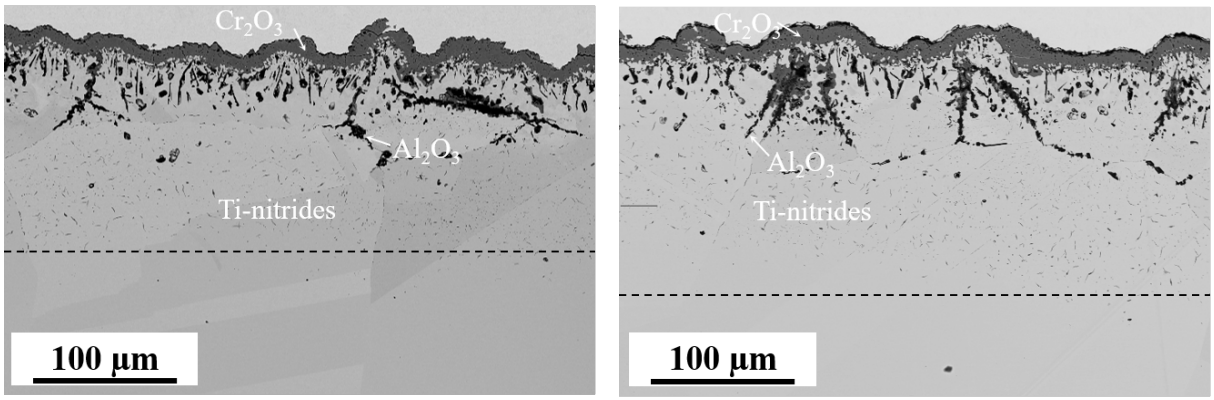

(a) (b)

Figure 12: BSE image of Ni-22Cr-Al-Ti after 500 h exposure in 1h-cycle (a) dry air and (b) air + 10 % H_2O at 950 °C.

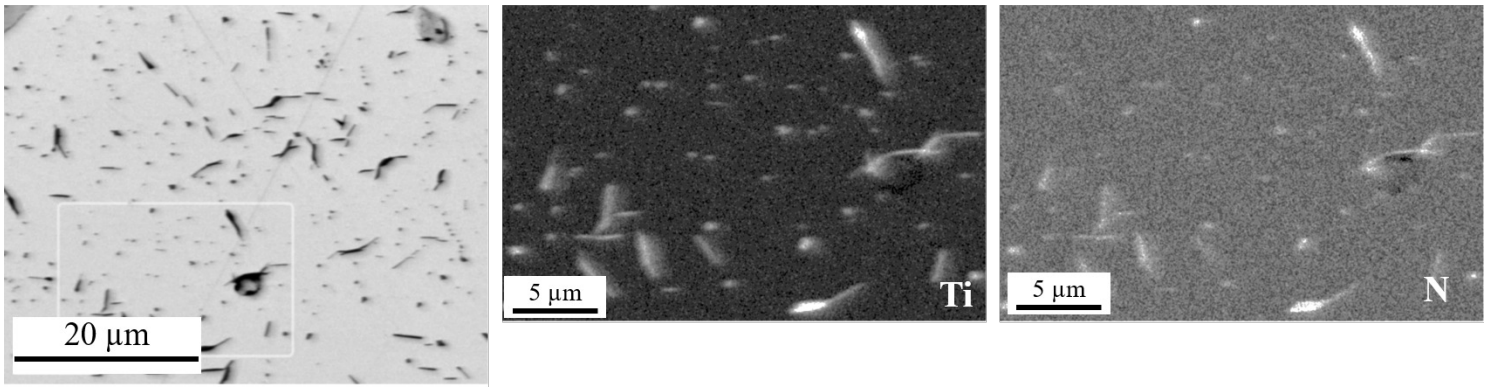

Figure 13: EDS elemental maps of Ti and Ni in the subsurface region of Ni-22Cr-Al-Ti after 500 h exposure in 1h-cycle dry air at 950 °C.

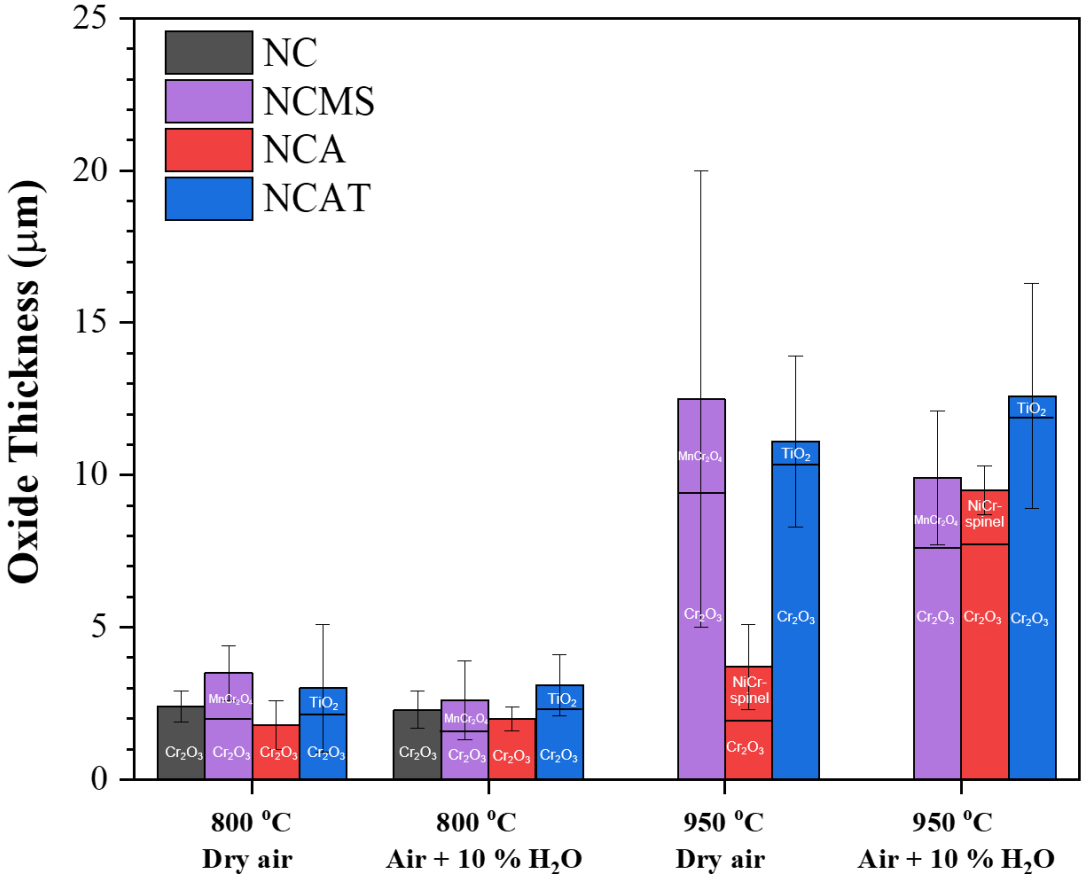

Figure 14: Thickness of oxide scales measured from BSE images using image analysis on the surface of Ni-22Cr, Ni-22Cr-Mn-Si, Ni-22Cr-2Al and Ni-22Cr-2Al-1Ti after 500 h exposure, 1h-cycle in dry air and air + 10 % H_2O at 800 and 950 °C.

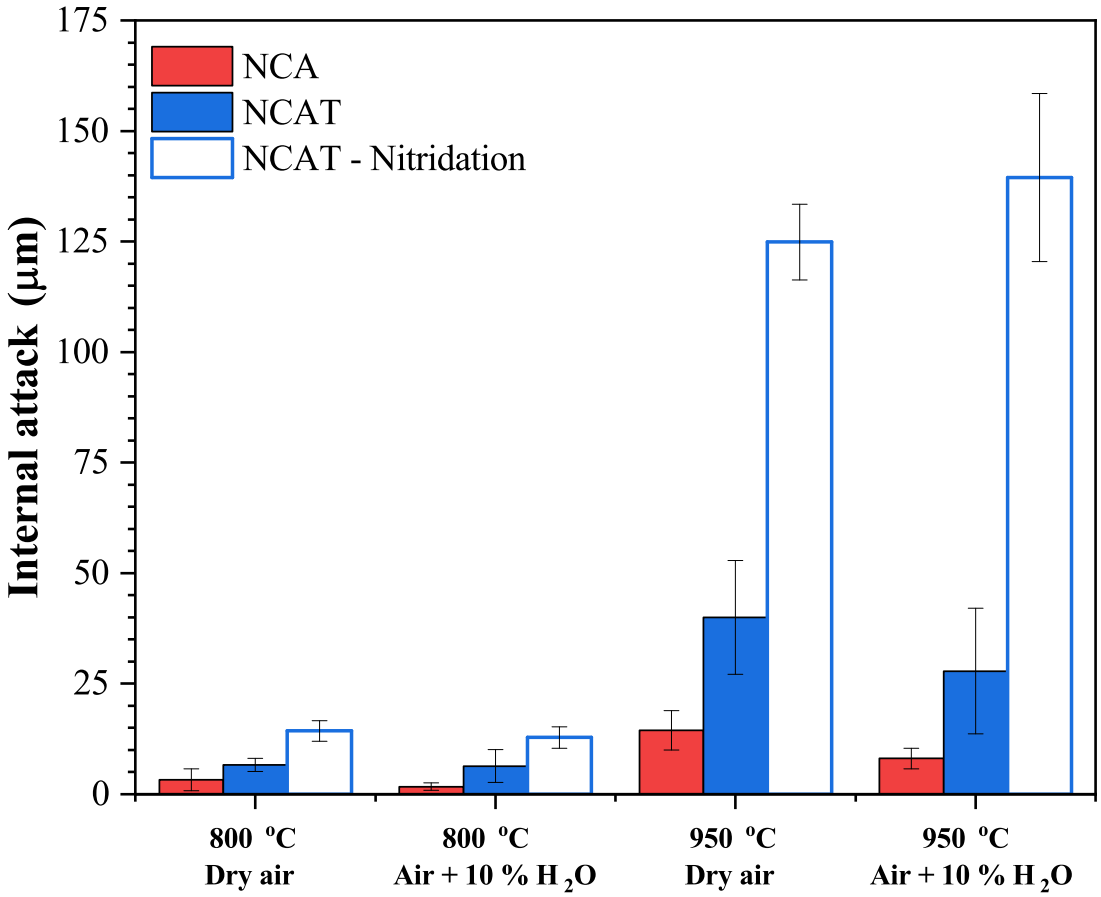

Figure 15: Depth of internal attack measured from BSE images using image analysis in Ni-22Cr-2Al (internal oxidation) and Ni-22Cr-2Al-1Ti (internal oxidation and nitridation) specimens after 500 h exposure in 1h-cycle dry air and air + 10 % H_2O at 800 and 950 °C.

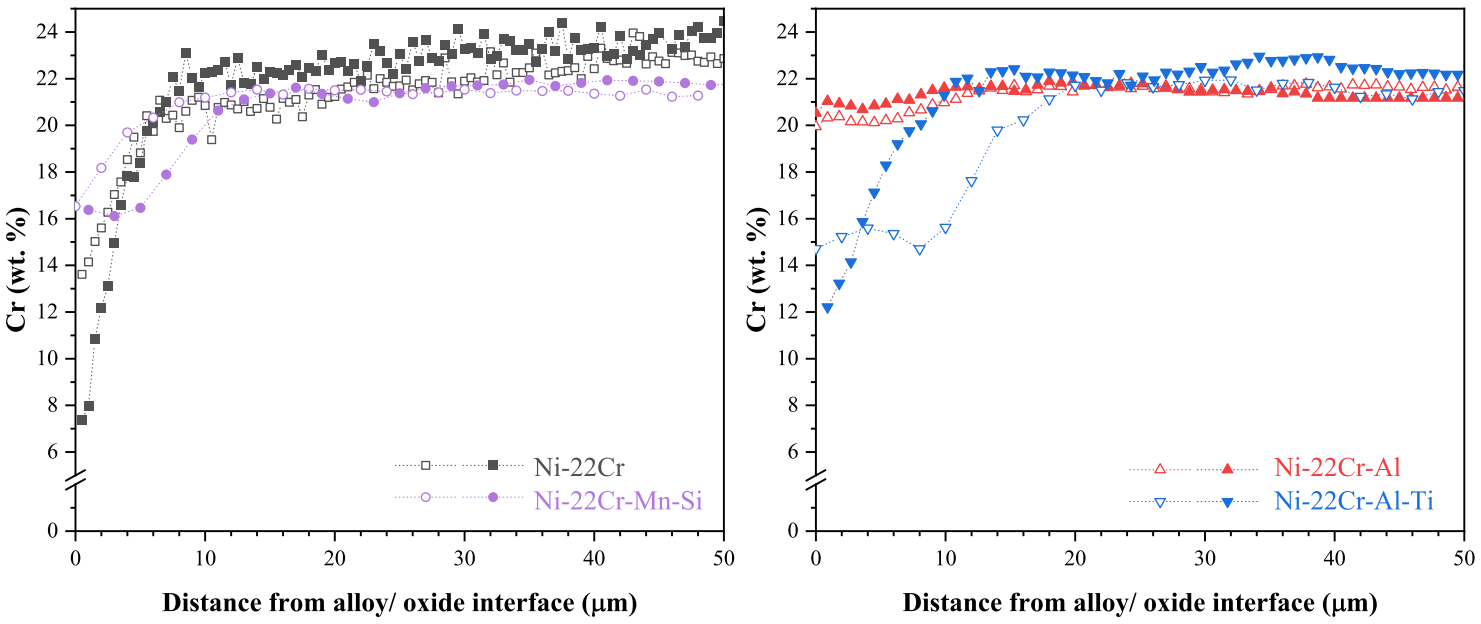

Figure 16: EDX Cr profiles of Ni-22Cr, Ni-22Cr-Mn-Si, Ni-22Cr-Al and Ni-22Cr-Al-Ti after 500 h exposure at 800 °C in 1h cycle (open symbols) dry air and (filled symbols) air + 10 % H_2O.

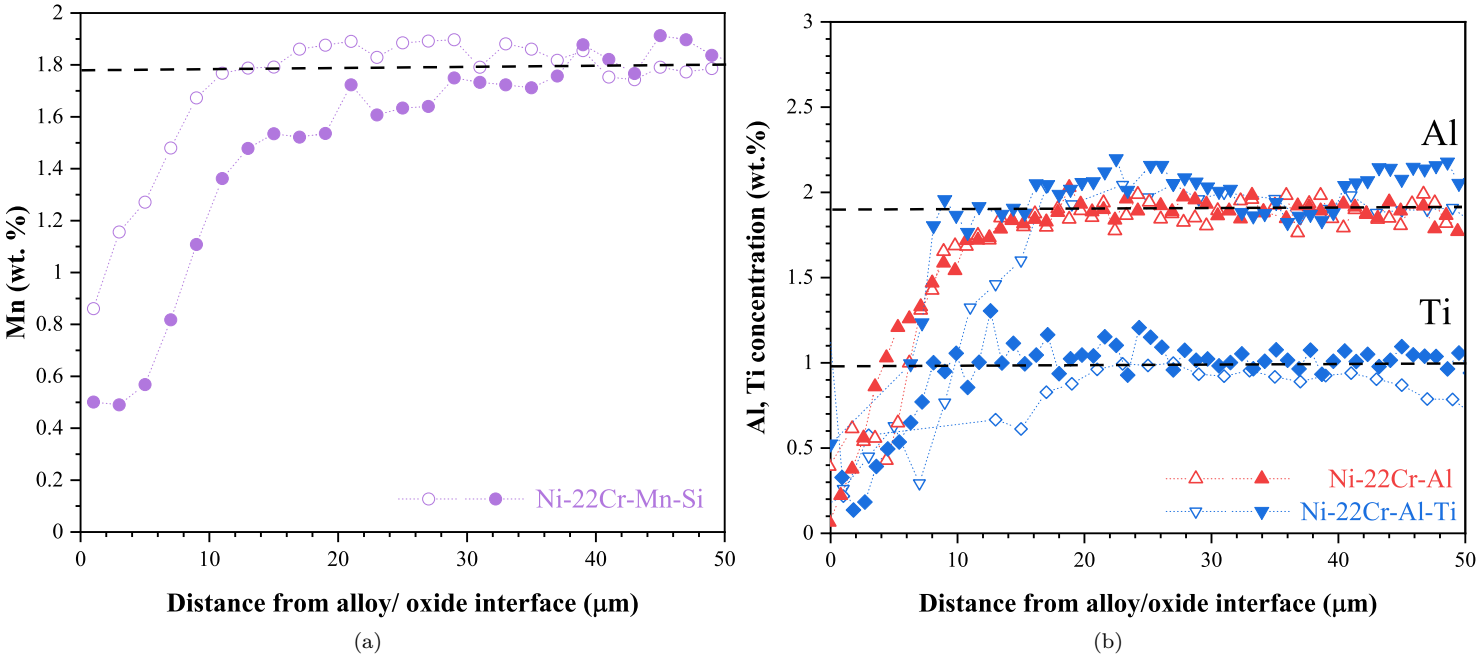

Figure 17: EDX (a) Mn and (b) Al and Ti profiles of Ni-22Cr-Mn-Si, Ni-22Cr-Al and Ni-22Cr-Al-Ti after 500 h exposure at 800 °C in 1h cycle (open symbols) dry air and (filled symbols) air + 10 % H_2O.

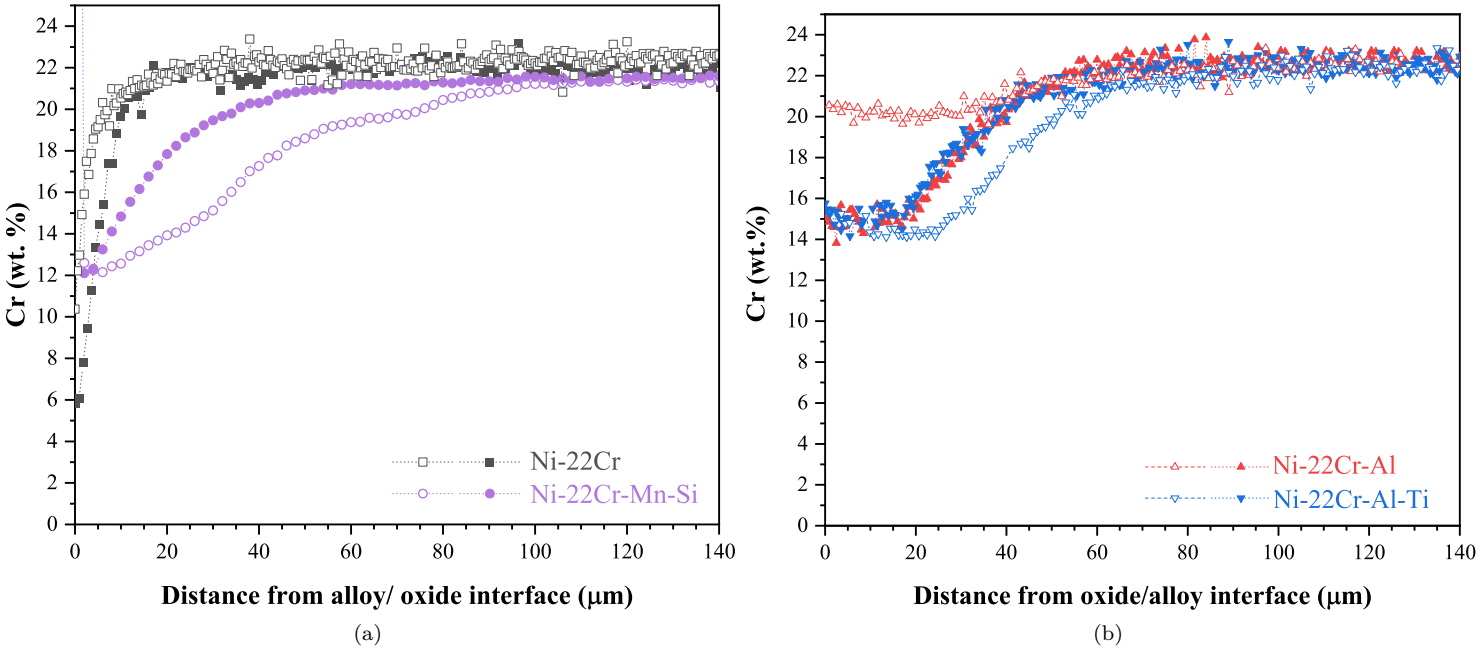

Figure 18: EDX Cr profiles of Ni-22Cr, Ni-22Cr-Mn-Si, Ni-22Cr-Al and Ni-22Cr-Al-Ti after 500 h exposure at 950 °C in 1h cycle (open symbols) dry air and (filled symbols) air + 10 % H_2O.

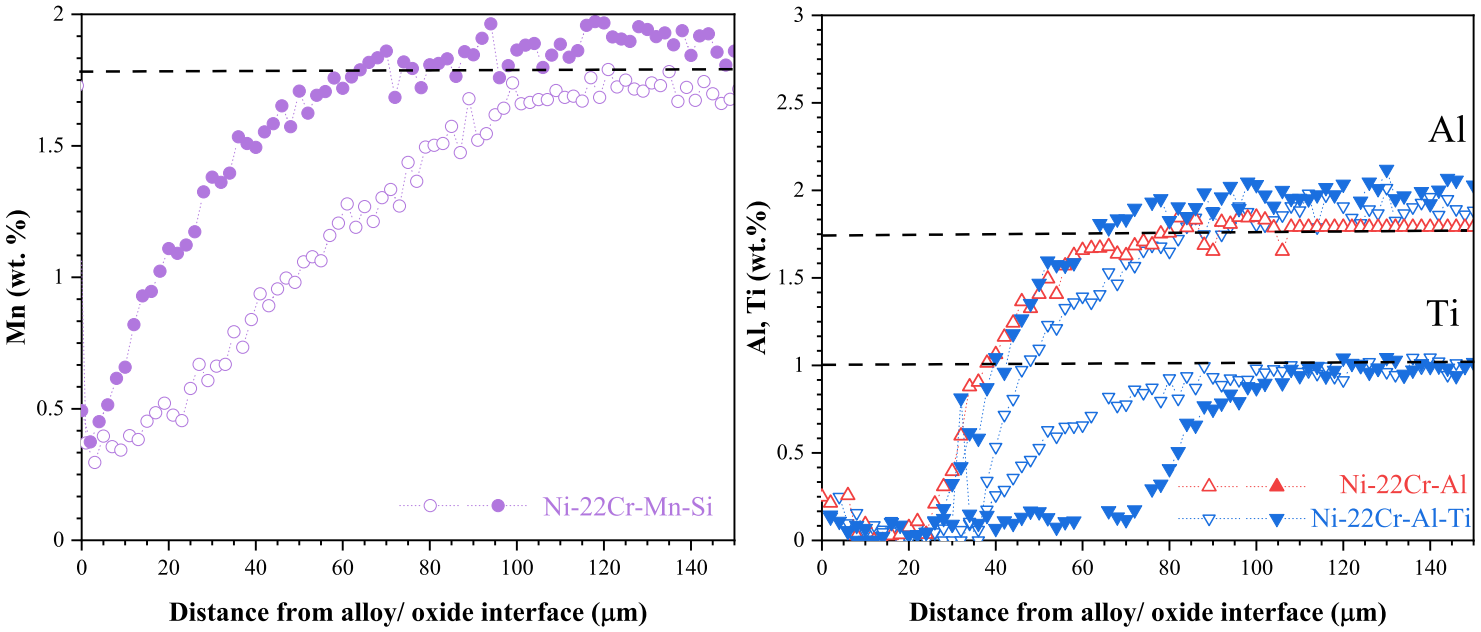

Figure 19: EDX (a) Mn and (b) Al profiles of Ni-22Cr-Mn-Si, Ni-22Cr-Al and Ni-22Cr-Al-Ti after 500 h exposure at 950 °C in 1h cycle (open symbols) dry air and (filled symbols) air + 10 % H_2O.

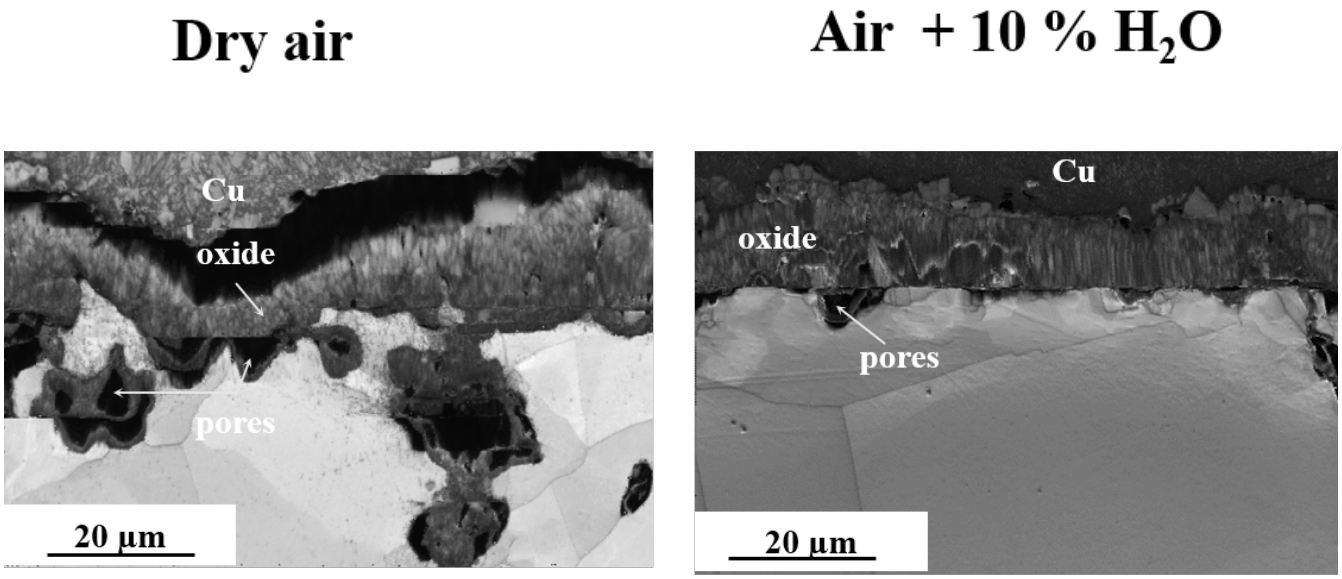

(a) Ni-22Cr-Mn-Si

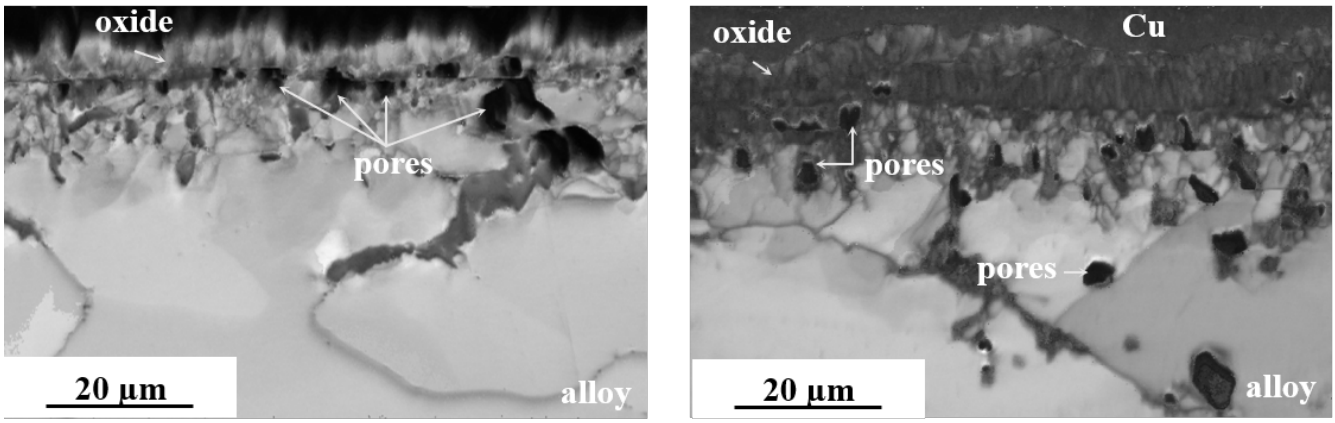

(b) Ni-22Cr-2Al

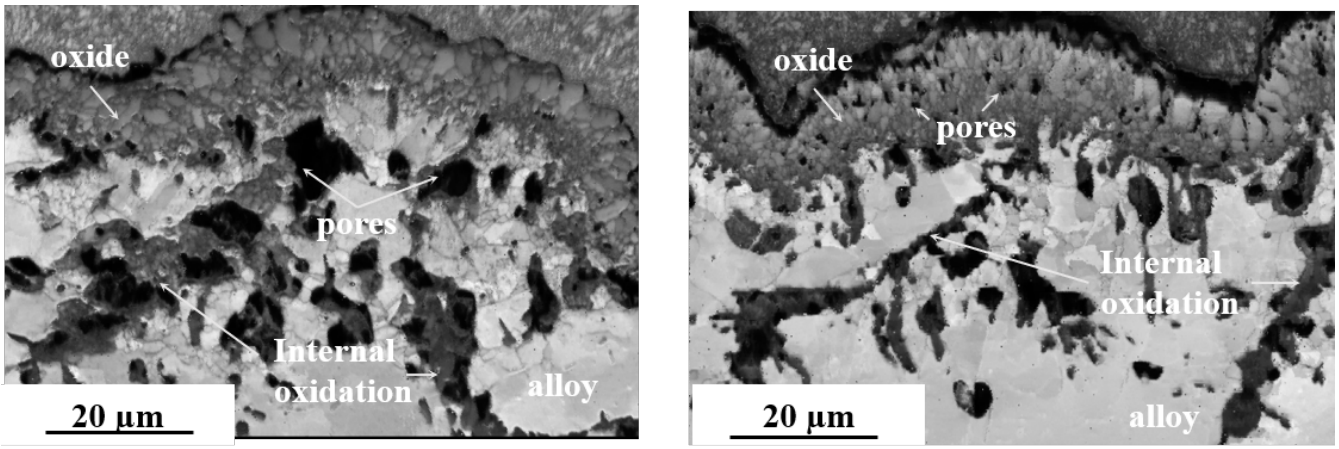

(c) Ni-22Cr-2Al-1Ti

Figure 20: EBSD band contrast images of oxide scale and subsurface microstructure of (a)Ni-22Cr-Mn-Si (b) Ni-22Cr-2Al and (c) Ni-22Cr-2Al-1Ti after 500 h exposure in 1h-cycle dry air and air + 10 % H_2O at 950 °C.

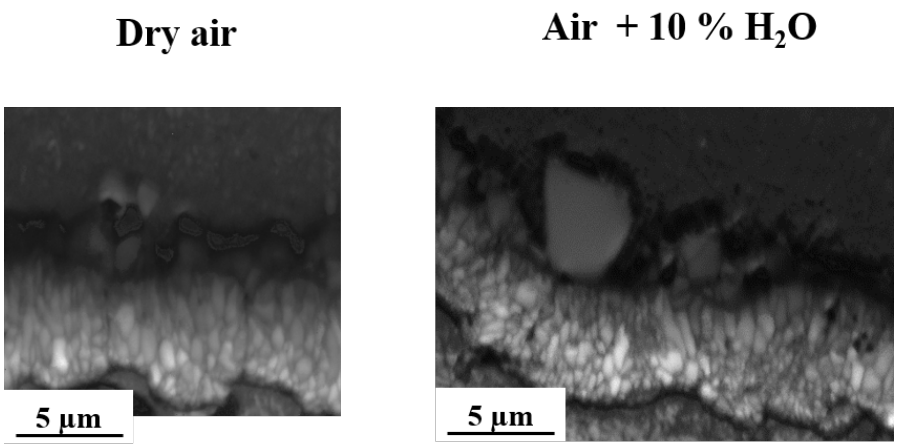

(a) Ni-22Cr-Mn-Si

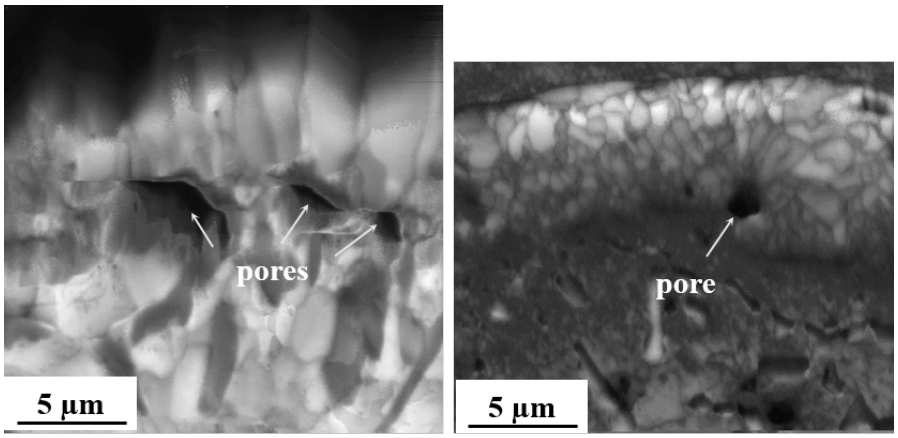

(b) Ni-22Cr-2Al

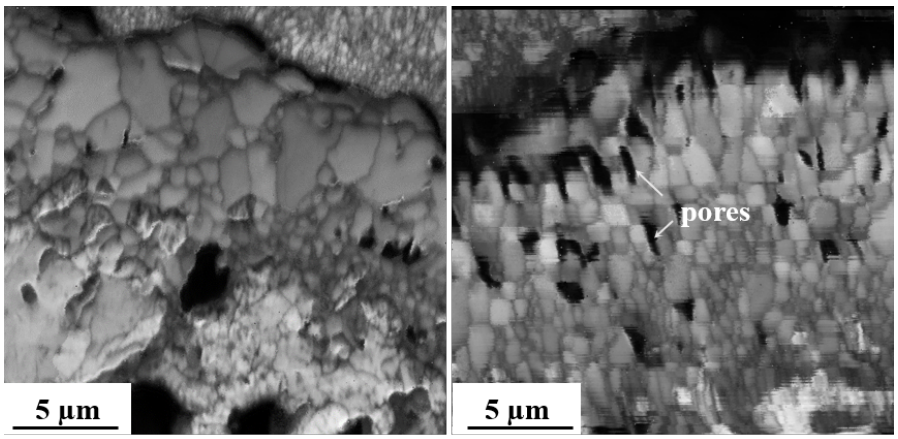

(c) Ni-22Cr-2Al-1Ti

Figure 21: EBSD Band contrast images at higher magnification of oxide scale of (a) Ni-22Cr-Mn-Si, (b) Ni-22Cr-2Al and (c) Ni-22Cr-2Al-1Ti after 500 h exposure in 1h-cycle dry air and air + 10 % H_2O at 950 °C.

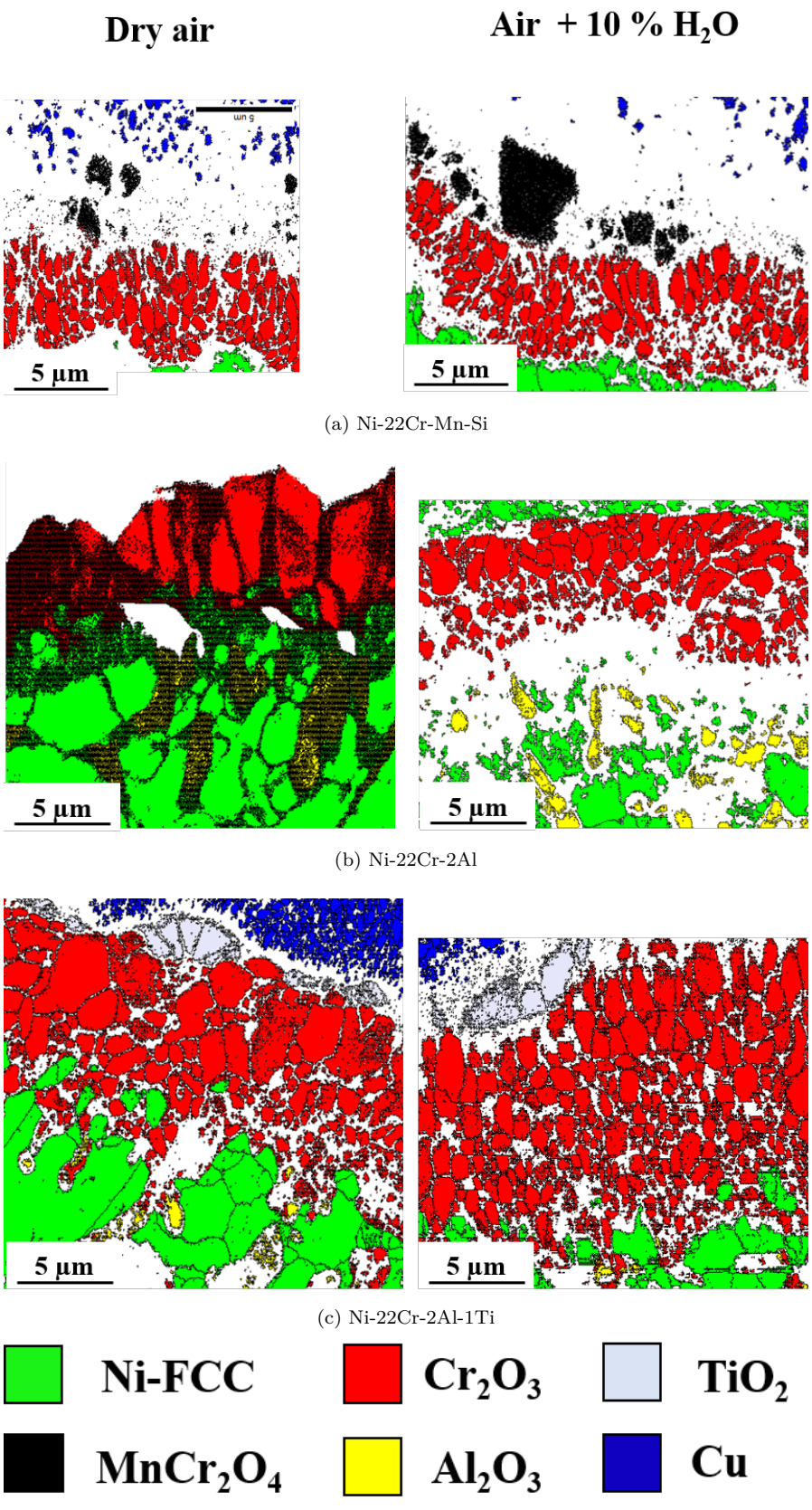

(a) Ni-22Cr-Mn-Si

(b) Ni-22Cr-2Al

(c) Ni-22Cr-2Al-1Ti

Figure 22: EBSD phase maps of oxide scale and subsurface microstructure of (a) Ni-22Cr-Mn-Si, (b) Ni-22Cr-2Al and (c) Ni-22Cr-2Al-1Ti after 500 h exposure in 1h-cycle dry air and air + 10 % H_2O at 950 °C.

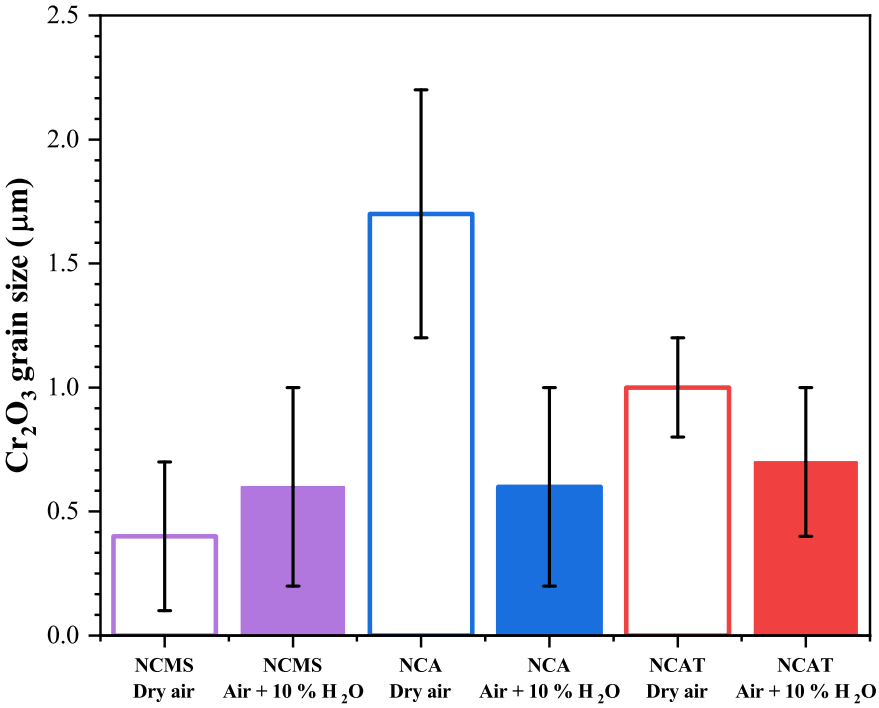

Figure 23: Cr_2O_3 grain size for Ni-22Cr-Mn-Si, Ni-22Cr-2Al and Ni-22Cr-2Al-1Ti alloys after 500 h exposure in 1h-cycle dry air and air + 10 % H_2O at 950 °C.

References

[1] D. Pierce, A. Haynes, J. Hughes, R. Graves, P. Maziasz, G. Muralidharan, A. Shyam, B. Wang, R. England, C. Daniel, High temperature materials for heavy duty diesel engines: Historical and future trends, Progress in Materials Science 103 (2019) 109 – 179. doi:https://doi.org/10.1016/j.pmatsci.2018.10.004.

[2] J. R. Davis, et al., ASM specialty handbook: heat-resistant materials, ASM International, 1997.

[3] J. Heywood, Internal Combustion Engine Fundamentals, McGraw-Hill Education, 1988.

[4] B. Gleeson, M. A. Harper, The long-term, cyclic-oxidation behavior of selected chromia-forming alloys, Oxidation of Metals 49 (3-4) (1998) 373–399.

[5] S. Osgerby, K. Berriche-Bouhanek, H. E. Evans, Tensile cracking of a chromia layer on a stainless steel during thermal cycling with hold periods, Materials Science and Engineering a-Structural Materials Properties Microstructure and Processing 412 (1-2) (2005) 182–190. doi:10.1016/j.msea.2005.08.193.

[6] V. P. Deodeshmukh, S. K. Srivastava, Long-term oxidation behavior of various chromia-forming alloys: Effect of thermal cycle length, in: ASME Turbo Expo 2009: Power for Land, Sea, and Air, American Society of Mechanical Engineers, 2009, pp. 885–892.

[7] H. Asteman, J.-E. Svensson, M. Norell, L.-G. Johansson, Influence of water vapor and flow rate on the high-temperature oxidation of 304l; effect of chromium oxide hydroxide evaporation, Oxidation of metals 54 (1-2) (2000) 11–26.

[8] E. J. Opila, D. L. Myers, N. S. Jacobson, I. M. B. Nielsen, D. F. Johnson, J. K. Olminsky, M. D. Allendorf, Theoretical and experimental investigation of the thermochemistry of $CrO_2(OH)_2$(g), Journal of Physical Chemistry A 111 (10) (2007) 1971–1980. doi:10.1021/jp0647380.

[9] G. Wood, D. Whittle, A comparison of the scaling behaviour of pure iron-chromium and nickel-chromium alloys in oxygen, Corrosion Science 6 (1966) 129–147. doi:10.1016/S0010-938X(66)80004-5.

[10] D. L. Douglass, J. S. Armijo, The effect of silicon and manganese on the oxidation mechanism of Ni-20 Cr, Oxidation of Metals 2 (2) (1970) 207–231. doi:10.1007/BF00603657.

[11] C. L. Angerman, Long-term oxidation of superalloys, Oxidation of Metals 5 (1972) 149–167. doi:10.1007/BF00610842.

[12] B. Li, B. Gleeson, Effects of silicon on the oxidation behavior of Ni-base chromia-forming alloys, Oxidation of Metals 65 (2006) 101–122. doi:10.1007/s11085-006-9003-4.

[13] J. Zurek, D. Young, E. Essuman, M. Hänsel, H. J. Penkalla, L. Niewolak, W. J. Quadakkers, Growth and adherence of chromia based surface scales on Ni-base alloys in high- and low-pO_2 gases, Materials Science and Engineering: A 477 (2008) 259–270. doi:10.1016/j.msea.2007.05.035.

[14] A. Chyrkin, P. Huczkowski, V. Shemet, L. Singheiser, W. J. Quadakkers, Sub-Scale Depletion and Enrichment Processes During High Temperature Oxidation of the Nickel Base Alloy 625 in the Temperature Range 900–1000 °C, Oxidation of Metals 75 (3-4) (2011) 143–166. doi:10.1007/s11085-010-9225-3.

[15] M. Hansel, L. Garcia-Fresnillo, S. L. Tobing, V. Shemet, Effect of H_2/H_2O ratio on thermally grown chromia scales formed on Ni25Cr alloy in Ar-H_2-H_2O atmospheres at 1000 degrees C, Materials at High Temperatures 29 (3) (2012) 187–192. doi:10.3184/096034012x13322698137785.

[16] D. Simon, B. Gorr, M. Hänsel, V. Shemet, H. J. Christ, W. J. Quadakkers, Effect of in-situ gas changes on thermally grown chromia scales formed on Ni–25Cr alloy at 1000°C in atmospheres with and without water vapour, Materials at High Temperatures 32 (1-2) (2015) 238–247. doi:10.1179/0960340914Z.000000000108.
URL https://doi.org/10.1179/0960340914Z.000000000108

[17] A. Jalowicka, R. Duan, P. Huczkowski, A. Chyrkin, D. Grüner, B. , K. Unocic, W. Quadakkers, Effect of Specimen Thickness on Microstructural Changes During Oxidation of the NiCrW Alloy 230 at 950–1050°C, Journal Of Metals 67 (2015) 2573–2588. doi:10.1007/s11837-015-1645-8.

[18] J. Meyer, V. Deodeshmukh, Long-Term Oxidation Resistance of Several Precipitation Strengthened Ni-Based Superalloys, in: ASME Turbo Expo 2017: Turbomachinery Technical Conference and Exposition, Vol. Volume 6: Ceramics; Controls,

Diagnostics and Instrumentation; Education; Manufacturing Materials and Metallurgy, V006T24A016. doi:10.1115/gt2017-64605.

[19] P. Huczkowski, W. Lehnert, H. H. Angermann, A. Chyrkin, R. Pillai, D. Gruner, E. Hejrani, W. J. Quadakkers, Effect of gas flow rate on oxidation behaviour of alloy 625 in wet air in the temperature range 900-1000 degrees C, Materials and Corrosion-Werkstoffe Und Korrosion 68 (2) (2017) 159–170. doi:10.1002/maco.201608831.

[20] B. A. Pint, R. Peraldi, P. J. Maziasz, The use of model alloys to develop corrosion-resistant stainless steels, High Temperature Corrosion and Protection of Materials 6, Prt 1 and 2, Proceedings 461-464 (2004) 815–822. doi:DOI10.4028/www.scientific.net/MSF.461-464.815.

[21] C. T. Rueden, J. Schindelin, M. C. Hiner, B. E. DeZonia, A. E. Walter, E. T. Arena, K. W. Eliceiri, ImageJ2: ImageJ for the next generation of scientific image data, BMC Bioinformatics 18 (1) (2017) 529. doi:10.1186/s12859-017-1934-z.

[22] F. H. Stott, Influence of alloy additions on oxidation, Materials Science and Technology 5 (8) (1989) 734–740. doi:DOI10.1179/mst.1989.5.8.734.

[23] X. Ledoux, S. Mathieu, M. Vilasi, Y. Wouters, P. Del-Gallo, M. Wagner, Oxide Growth Characterization During Short-Time Oxidation of a Commercially Available Chromia-Forming Alloy (HR-120) in Air at 1,050 degrees C, Oxidation of Metals 80 (1-2) (2013) 25–35. doi:10.1007/s11085-013-9367-1.

[24] T. Perez, L. Latu-Romain, R. Podor, J. Lautru, Y. Parsa, S. Mathieu, M. Vilasi, Y. Wouters, In Situ Oxide Growth Characterization of Mn-Containing Ni-25Cr (wt.%) Model Alloys at 1050 degrees C, Oxidation of Metals 89 (5-6) (2018) 781–795. doi:10.1007/s11085-017-9819-0.

[25] D. Kim, C. Jang, W. S. Ryu, Oxidation Characteristics and Oxide Layer Evolution of Alloy 617 and Haynes 230 at 900 °C and 1100 °C, Oxidation of Metals 71 (5) (2009) 271–293. doi:10.1007/s11085-009-9142-5.

[26] D. J. Young, B. A. Pint, Chromium volatilization rates from Cr_2O_3 scales into flowing gases containing water vapor, Oxidation of Metals 66 (3-4) (2006) 137–153. doi:10.1007/s11085-006-9030-1.

[27] R. E. Lobnig, H. P. Schmidt, K. Hennesen, H. J. Grabke, Diffusion of Cations in Chromia Layers Grown on Iron-Base Alloys, Oxidation of Metals 37 (1-2) (1992) 81–93. doi:10.1007/bf00665632.

[28] M. J. Bennett, J. B. Price, A Physical and Chemical Examination of an Ethylene Steam Cracker Coke and of the Underlying Pyrolysis Tube, Journal of Materials Science 16 (1) (1981) 170–188. doi:Doi10.1007/Bf00552071.

[29] H. E. Evans, D. A. Hilton, R. A. Holm, S. J. Webster, Influence of Silicon Additions on the Oxidation Resistance of a Stainless-Steel, Oxidation of Metals 19 (1-2) (1983) 1–18. doi:Doi10.1007/Bf00656225.

[30] A. Vayyala, I. Povstugar, D. Naumenko, W. J. Quadakkers, H. Hattendorf, J. Mayer, A Nanoscale Study of Thermally Grown Chromia on High-Cr Ferritic Steels and Associated Oxidation Mechanisms, Journal of the Electrochemical Society 167 (6) (2020). doi:ARTN06150210.1149/1945-7111/ab7d2e.

[31] J. S. Armijo, The kinetics and mechanism of solid-state spinel formation — A review and critique, Oxidation of Metals 1 (2) (1969) 171–198. doi:10.1007/BF00603514.

[32] C. S. Giggins, F. S. Pettit, Oxidation of Ni-Cr-Al Alloys between 1000 Degrees and 1200 Degrees C, Journal of the Electrochemical Society 118 (11) (1971) 1782–1790.

[33] A. Chyrkin, R. Pillai, T. Galiullin, E. Wessel, D. Gruner, W. J. Quadakkers, External alpha-Al_2O_3 scale on Ni-base alloy 602 CA. - Part I: Formation and long-term stability, Corrosion Science 124 (2017) 138–149. doi:10.1016/j.corsci.2017.05.017.

[34] G. Hultquist, B. Tveten, E. Hornlund, Hydrogen in chromium: Influence on the high-temperature oxidation kinetics in H2O, oxide-growth mechanisms, and scale adherence, Oxidation of Metals 54 (1-2) (2000) 1–10. doi:Doi10.1023/A:1004610626903.

[35] M. Michalik, M. Hansel, J. Zurek, L. Singheiser, W. J. Quadakkers, Effect of water vapour on growth and adherence of chromia scales formed on Cr in high and low pO_2-environments at 1000 and 1050°C, Materials at High Temperatures 22 (3-4) (2005) 213–221.

[36] M. Hansel, W. J. Quadakkers, D. J. Young, Role of water vapor in chromia-scale growth at low oxygen partial pressure, Oxidation of Metals 59 (3-4) (2003) 285–301.
URL <GotoISI>://WOS:000182551100005

[37] D. Whittle, D. Evans, D. Scully, G. Wood, Compositional changes in the underlying alloy during the protective oxidation of alloys, Acta Metallurgica 15 (9) (1967) 1421 – 1430. doi:https://doi.org/10.1016/0001-6160(67)90173-3.

[38] A. Chyrkin, R. Pillai, H. Ackermann, H. Hattendorf, S. Richter, W. Nowak, D. Grüner, W. Quadakkers, Modeling carbide dissolution in alloy 602 ca during high temperature oxidation, Corrosion Science 96 (2015) 32–41. doi:10.1016/j.corsci.2015.03.019.

[39] J. H. Chen, P. M. Rogers, J. A. Little, Oxidation behavior of several chromia-forming commercial nickel-base superalloys, Oxidation of Metals 47 (5) (1997) 381–410. doi:10.1007/BF02134783.

[40] A. S. Nagelberg, Oxidation of Titanium Modified Type-310 Stainless-Steel in Low Oxygen Partial-Pressure Atmospheres, Oxidation of Metals 17 (5-6) (1982) 415–427. doi:Doi10.1007/Bf00742121.

[41] E. Essuman, L. R. Walker, J. Maziasz, B. A. Pint, Oxidation behaviour of cast ni-cr alloys in steam at 800 degrees c, Materials Science and Technology 29 (7) (2013) 822–827. doi:10.1179/1743284712y.0000000103.

[42] A. Naoumidis, H. A. Schulze, C. Garciarosales, Phase Studies in the System Chromium-Manganese-Titanium Oxide at Different Oxygen Partial Pressures, Epdic 1 : European Powder Diffraction, Pts 1 and 2 79 (1991) 691–695.

[43] P. Kofstad, High Temperature Corrosion, Elsevier Applied Science, 1988.

[44] A. Holt, P. Kofstad, Electrical conductivity of Cr_2O_3 doped with TiO_2, Solid State Ionics 117 (1-2) (1999) 21–25. doi:Doi10.1016/S0167-2738(98)00244-6.

[45] M. Michalik, S. L. Tobing, M. Hansel, V. Shemet, W. J. Quadakkers, D. J. Young, Effects of water vapour on the high temperature nitridation of chromium, Materials and Corrosion-Werkstoffe Und Korrosion 65 (3) (2014) 260–266. doi:10.1002/maco.201307160.
URL <GotoISI>://WOS:000332338100003

[46] A. Jalowicka, W. Nowak, D. J. Young, V. Nischwitz, D. Naumenko, W. J. Quadakkers, Boron Depletion in a Nickel Base Superalloy Induced by High Temperature Oxidation, Oxidation of Metals 83 (3-4) (2015) 393–413.

[47] W. J. Nowak, P. Wierzba, D. Naumenko, W. J. Quadakkers, J. Sieniawski, Water vapour effect on high temperature oxidation behaviour of superalloy Rene 80, Advances in Manufacturing Science and Technology 40 (2016) 41–52.

[48] U. Krupp, H. J. Christ, Internal nitridation of nickel-base alloys. Part II. Behavior of quaternary Ni-Cr-Al-Ti alloys and computer-based description, Oxidation of Metals 52 (3-4) (1999) 299–320. doi:Doi10.1023/A:1018895628849.